

Wave evolution over submerged sills: tests of a high-order Boussinesq model

Maurício F. Gobbi¹, James T. Kirby^{*}

Center for Applied Coastal Research, Ocean Engineering Laboratory, University of Delaware, Newark, DE 19716, USA

Received 28 July 1998; received in revised form 20 January 1999; accepted 4 February 1999

Abstract

A Boussinesq model accurate to $O(\mu)^4$, $\mu = k_0 h_0$ in dispersion and retaining all nonlinear effects is derived for the case of variable water depth. A numerical implementation of the model in one horizontal direction is described. An algorithm for wave generation using a grid-interior source function is derived. The model is tested in its complete form, in a weakly nonlinear form corresponding to the approximation $\delta = O(\mu^2)$, $\delta = a/h_0$, and in a fully nonlinear form accurate to $O(\mu^2)$ in dispersion [Wei, G., Kirby, J.T., Grilli, S.T., Subramanya R. (1995). A fully nonlinear Boussinesq model for surface waves: Part 1. Highly nonlinear unsteady waves. *J. Fluid Mech.*, 294, 71–92]. Test cases are taken from the experiments described by Dingemans [Dingemans, M.W. (1994). Comparison of computations with Boussinesq-like models and laboratory measurements. Report H-1684.12, Delft Hydraulics, 32 pp.] and Ohyaama et al. [Ohyaama, T., Kiota, W., Tada, A. (1994). Applicability of numerical models to nonlinear dispersive waves. *Coastal Engineering*, 24, 297–313.] and consider the shoaling and disintegration of monochromatic wave trains propagating over an elevated bar feature in an otherwise constant depth tank. Results clearly demonstrate the importance of the retention of fully-nonlinear effects in correct prediction of the evolved wave fields. © 1999 Elsevier Science B.V. All rights reserved.

Keywords: Boussinesq model; Wave field; Depth tank

^{*} Corresponding author. Tel.: +1-302-831-2438; Fax: +1-302-831-1228; E-mail: kirby@udel.edu

¹ Present address: Sistema Meteorológico do Parana, Caixa Postal 318, 80001-970 Curitiba PR, Brazil. E-mail: gobbi@simepar.br.

1. Introduction

Great strides have been made in the recent past to extend the range of applicability of Boussinesq-type equations for surface water wave propagation and bring them into the family of operational coastal wave prediction models. Most of the initial recent work in this area has centered on the notion that the primary avenue of improvement would be to correct the model's apparent linear dispersion characteristics by means of a reorganization of dispersive (or $O(\mu^2)$, where μ denotes the water depth to wavelength ratio) terms, thereby extending the range of water depths in which a wave of a given frequency could be modelled with reasonable accuracy. Madsen et al. (1991) and Madsen and Sørensen (1992) achieved this goal in a depth-integrated model by simple rearrangement of dispersive terms, while Nwogu (1993) achieved a similar result by redefinition of the dependent velocity variable. Either approach led to models with linear dispersion relations which can be written in the form

$$\omega^2 = gk^2 h \frac{1 - \left(\alpha + \frac{1}{3} \right) (kh)^2}{1 - \alpha (kh)^2} \quad (1)$$

where the choice $\alpha = -2/5$ produces the (2,2) Padé approximant of the full dispersion relation. Models of this type have been extensively tested for their applicability to the prediction of nearshore wave height and wave-induced circulation, as detailed in a recent series of papers by Madsen et al. (1997a,b) and Sørensen et al. (1998).

Subsequently, Kirby and Wei (1994) argued that models based on such an extension to the linear formulation may not be producing a better nonlinear model in the extended region, since the absence of dispersive modifications to nonlinear terms destroyed the consistent ordering of coefficients in Stokes-type expansions of the model equations. The results indicated that models retaining nonlinear effects to all orders resulting from a direct application of the form of the velocity field obtained at any order in the dispersion parameter $\mu = k_0 h_0$ would produce a more consistent picture of nonlinear behavior both in the long wave limit and in the intermediate depth range being investigated. Models of this type would drop the standard scaling assumption $\delta = O(\mu^2)$, where $\delta = a/h_0$ denotes a height-to-depth ratio characterising nonlinear effects. Such a model, retaining dispersion to $O(\mu^2)$ and all corresponding nonlinear effects, was developed by Wei et al. (1995) and shown to be a much more accurate predictor of solitary wave shoaling than the weakly-nonlinear model of Nwogu (1993). The accuracy of that model as a predictor of Stokes-type solutions is documented in (Kirby and Wei, 1994) as well as in the companion paper to the present contribution, Gobbi et al. (1998b), hereafter referred to as GKW98. These earlier results demonstrate the defects in corresponding Stokes wave solutions for weakly nonlinear models in the asymptotic approach to the shallow water limit. Models in the $O(\mu^2)$, fully-nonlinear formulation have also been extensively tested for their applicability to the modelling of nearshore waves and currents; see a recent example by Chen et al. (1999).

Recently, GKW98 have extended the formulation of the fully-nonlinear Boussinesq-type model to $O(\mu^4)$, using a model based on kinematic flow-field information to the

same order of approximation. The model has been tested both in the intermediate-depth, Stokes-wave regime and in the shallow water, solitary wave regime, where convergence to the full solution of Tanaka (1986) was demonstrated with increasing level of approximation in powers of μ^2 .

In the present paper, we present a numerical solution technique for the $O(\mu^4)$ GKW98 model and apply it to the study of wave propagation and harmonic decomposition over an isolated shoal. Particular attention is paid to the question of whether the most important feature retained in the final model is the fully-nonlinear property (relative to a weakly nonlinear model at $O(\mu^4)$), or the incorporation of enhanced linear dispersion going from the $O(\mu^2)$ fully-nonlinear model of Wei et al. (1995) to the $O(\mu^4)$ fully-nonlinear model of GKW98. Laboratory data is taken from two sets of experiments, one (Dingemans, 1994) describing wave propagation over a gradual shoal mimicking a natural bar formation, and one (Ohyama et al., 1994) describing wave propagation over an abrupt feature reminiscent of an artificial submerged breakwater. A detailed comparison between model predictions and laboratory data is given for each case.

2. Derivation of fourth-order fully nonlinear model

In this section, we derive a fully nonlinear Boussinesq-type model based on a 4th order vertical polynomial for the velocity potential, extending the work of GKW98 to the variable depth case. A set of equations for a velocity-type variable is then given. We assume the fluid is inviscid and incompressible, and the flow is irrotational, so that a velocity potential ϕ exists and the velocity field can be written as

$$\mathbf{u} = \nabla_3 \phi, \quad (2)$$

where the fluid velocity vector $\mathbf{u} \equiv (u, v, w)$, and ϕ are functions of the spatial Cartesian coordinates x, y, z and time t , and ∇_3 is the three dimensional gradient operator $\nabla_3 \equiv (\partial/\partial x, \partial/\partial y, \partial/\partial z)$.

The full boundary value problem for potential flow is given in terms of nondimensional variables by

$$\phi_{zz} + \mu^2 \nabla^2 \phi = 0, \quad -h \leq z \leq \delta\eta; \quad (3)$$

$$\phi_z + \mu^2 \nabla h \cdot \nabla \phi = 0, \quad z = -h; \quad (4)$$

$$\eta + \phi_t + \frac{1}{2} \delta \left[(\nabla \phi)^2 + \frac{1}{\mu^2} (\phi_z)^2 \right] = 0, \quad z = \delta\eta; \quad (5)$$

$$\eta_t + \delta \nabla \phi \cdot \nabla \eta - \frac{1}{\mu^2} \phi_z = 0, \quad z = \delta\eta; \quad (6)$$

x and y are the horizontal coordinates scaled by a representative wave number $k_0 = 2\pi/L_0$, where L_0 is a wave length, z is the vertical coordinate starting at the still water level and pointing upwards and h is the water depth, both scaled by a typical

depth h_0 . η is the water surface displacement scaled by a representative amplitude a_0 . Two dimensionless parameters are apparent: $\delta = a_0/h_0$ and $\mu^2 = (k_0 h_0)^2$. Time t is scaled by $(k_0(g h_0)^{1/2})^{-1}$, and ϕ , the velocity potential, is scaled by $\delta h_0 (g h_0)^{1/2}$. g is the acceleration due to the gravitational field, and ∇ is the two-dimensional horizontal (x,y) gradient operator.

Integrating Eq. (3) over the water column and using Eqs. (4) and (6), we obtain a mass conservation equation

$$\eta_t + \nabla \cdot \mathbf{M} = 0, \quad \mathbf{M} = \int_{-h}^{\delta \eta} \nabla \phi \, dz. \tag{7}$$

We now proceed to derive model equations for waves over an arbitrary bottom $h(x,y)$, and assuming $\delta = O(1)$ and $O(\mu^2) \ll 1$. We assume an N th degree polynomial approximation for ϕ in the z coordinate

$$\phi = \sum_{n=0}^N \zeta^n \phi_n(x, y, t), \tag{8}$$

where

$$\zeta = (h + z), \tag{9}$$

and ϕ_n are functions of the horizontal spatial coordinates and time. By taking the limit of Eq. (8) as $\zeta \rightarrow 0$, it is clear that ϕ_0 is the velocity potential at the bottom $\zeta = 0$. Substituting Eq. (8) into Eq. (4), we obtain an expression for ϕ_1 in terms of ϕ_0

$$\phi_1 = -\mu^2 G \nabla h \cdot \nabla \phi_0, \tag{10}$$

where $G \equiv (1 + \mu^2 |\nabla h|^2)^{-1}$. Since we are seeking an asymptotic approximation for ϕ in terms of the small parameter μ^2 , it would be consistent if we expanded G in a binomial expansion around $\mu^2 = 0$. However, we choose not to do this in order to maintain the positive definiteness of this quantity as the bottom slope becomes steep. Substituting Eq. (8) into Eq. (3), and equating coefficients of like powers of ζ to zero, we obtain the following recursion formula

$$\begin{aligned} (n+2)(n+1)\phi_{n+2} + \mu^2 \left[(n+2)(n+1) |\nabla h|^2 \phi_{n+2} + (n+1) \nabla^2 h \phi_{n+1} \right. \\ \left. + 2(n+1) \nabla h \cdot \nabla \phi_{n+1} + \nabla^2 \phi_n \right] = 0. \end{aligned} \tag{11}$$

We now use Eqs. (10) and (11) to obtain the ϕ_n in terms of ϕ_0 . The series is truncated at $n = 4$, yielding

$$\begin{aligned} \phi = \phi_0 - \mu^2 \left(G \nabla h \cdot \nabla \phi_0 \zeta + \frac{1}{2} G \nabla^2 \phi_0 \zeta^2 \right) \\ + \mu^4 \left\{ \left[\frac{1}{2} G^2 \nabla^2 h \nabla h \cdot \nabla \phi_0 + G \nabla h \cdot \nabla (G \nabla h \cdot \nabla \phi_0) \right] \zeta^2 \right. \\ + \left[\frac{1}{6} G^2 \nabla^2 h \nabla^2 \phi_0 + \frac{1}{3} G \nabla h \cdot \nabla (G \nabla^2 \phi_0) + \frac{1}{6} G \nabla^2 (G \nabla h \cdot \nabla \phi_0) \right] \zeta^3 \\ \left. + \frac{1}{24} G \nabla^2 (G \nabla^2 \phi_0) \zeta^4 \right\}. \end{aligned} \tag{12}$$

Commensurate with the extension of the velocity potential to $O(\mu^4)$, we seek to derive a set of model equations having a corresponding dispersion relationship in the form of a (4,4) Padé approximant representing the approximation

$$\frac{\tanh \mu}{\mu} \approx \frac{1 + (1/9)\mu^2 + (1/945)\mu^4}{1 + (4/9)\mu^2 + (1/63)\mu^4} + O(\mu^6). \tag{13}$$

Following GKW98, we define a new dependent variable

$$\tilde{\phi} = \beta\phi_a + (1 - \beta)\phi_b \tag{14}$$

where ϕ_a and ϕ_b are the velocity potentials at elevations $z = z_a$ and $z = z_b$, and β is a weight parameter. Relationships between these parameters to give the appropriate dispersion relationship were obtained by GKW98 and are given by

$$z_a = \left[\frac{1}{9} - \left\{ \frac{8\beta}{567(1-\beta)} \right\}^{1/2} + \left\{ \frac{8}{567\beta(1-\beta)} \right\}^{1/2} \right]^{1/2} - 1, \tag{15}$$

$$z_b = \left[\frac{1}{9} - \left\{ \frac{8\beta}{567(1-\beta)} \right\}^{1/2} \right]^{1/2} - 1, \tag{16}$$

with $0.018 \leq \beta \leq 0.467$. Although the free parameter β can be calibrated to give better linear shoaling characteristics, we found that variations of β within the limits above had little effect on the actual fully nonlinear numerical solution, at least for the cases tested, and we used the value $\beta = 0.2$ throughout this work.

$\tilde{\phi}$ may be written in terms of ϕ_0 using Eq. (12) yielding

$$\begin{aligned} \tilde{\phi} = & \phi_0 - \mu^2 \left(AhG\nabla h \cdot \nabla\phi_0 + \frac{1}{2}Bh^2G\nabla^2\phi_0 \right) \\ & + \mu^4 \left\{ Bh^2 \left[\frac{1}{2}G^2\nabla^2h\nabla h \cdot \nabla\phi_0 + G\nabla h \cdot \nabla(G\nabla h \cdot \nabla\phi_0) \right] \right. \\ & + Ch^3 \left[\frac{1}{6}G^2\nabla^2h\nabla^2\phi_0 + \frac{1}{3}G\nabla h \cdot \nabla(G\nabla^2\phi_0) + \frac{1}{6}G\nabla^2(G\nabla h \cdot \nabla\phi_0) \right] \\ & \left. + \frac{1}{24}Dh^4G\nabla^2(G\nabla^2\phi_0) \right\}, \end{aligned} \tag{17}$$

where

$$A \equiv \frac{1}{h} \left[\beta(h + z_a) + (1 - \beta)(h + z_b) \right], \tag{18}$$

$$B \equiv \frac{1}{h^2} \left[\beta(h + z_a)^2 + (1 - \beta)(h + z_b)^2 \right], \tag{19}$$

$$C \equiv \frac{1}{h^3} \left[\beta(h + z_a)^3 + (1 - \beta)(h + z_b)^3 \right], \tag{20}$$

$$D \equiv \frac{1}{h^4} \left[\beta(h + z_a)^4 + (1 - \beta)(h + z_b)^4 \right], \tag{21}$$

Inverting Eq. (17) gives a formula for ϕ_0 in terms of $\tilde{\phi}$ which is substituted into Eq. (12), leading to an approximation to the full velocity potential in terms of $\tilde{\phi}$

$$\begin{aligned} \phi = & \tilde{\phi} + \mu^2 \left[(Ah - \zeta) F_1(\tilde{\phi}) + (Bh^2 - \zeta^2) F_2(\tilde{\phi}) \right] + \mu^4 \left[(Ah - \zeta) F_3(\tilde{\phi}) \right. \\ & \left. + (Bh^2 - \zeta^2) F_4(\tilde{\phi}) + (Ch^3 - \zeta^3) F_5(\tilde{\phi}) + (Dh^4 - \zeta^4) F_6(\tilde{\phi}) \right], \end{aligned} \quad (22)$$

where

$$F_1(\tilde{\phi}) \equiv G \nabla h \cdot \nabla \tilde{\phi}, \quad (23)$$

$$F_2(\tilde{\phi}) \equiv \frac{1}{2} G \nabla^2 \tilde{\phi}, \quad (24)$$

$$F_3(\tilde{\phi}) \equiv \nabla h \cdot \nabla (Ah \nabla h \cdot \nabla \tilde{\phi}) + \frac{1}{2} \nabla h \cdot \nabla (Bh^2 \nabla^2 \tilde{\phi}), \quad (25)$$

$$\begin{aligned} F_4(\tilde{\phi}) \equiv & \frac{1}{2} \nabla^2 (Ah \nabla h \cdot \nabla \tilde{\phi}) + \frac{1}{4} \nabla^2 (Bh^2 \nabla^2 \tilde{\phi}) - \frac{1}{2} \nabla^2 h \nabla h \cdot \nabla \tilde{\phi} \\ & - \nabla h \cdot \nabla (\nabla h \cdot \nabla \tilde{\phi}), \end{aligned} \quad (26)$$

$$F_5(\tilde{\phi}) \equiv -\frac{1}{6} \nabla^2 h \nabla^2 \tilde{\phi} - \frac{1}{3} \nabla h \cdot \nabla (\nabla^2 \tilde{\phi}) - \frac{1}{6} \nabla^2 (\nabla h \cdot \nabla \tilde{\phi}), \quad (27)$$

$$F_6(\tilde{\phi}) \equiv -\frac{1}{24} \nabla^2 (\nabla^2 \tilde{\phi}), \quad (28)$$

By substituting Eq. (22) into Eq. (7) and neglecting terms of $O(\mu^6)$ and higher, we obtain the approximate mass flux

$$\begin{aligned} \mathbf{M} = & H \nabla \tilde{\phi} + \mu^2 H \left\{ \left[(A - 1) F_1(\tilde{\phi}) + 2 \left(Bh - \frac{H}{2} \right) F_2(\tilde{\phi}) \right] \nabla h \right. \\ & \left. + \left(Ah - \frac{H}{2} \right) \nabla F_1(\tilde{\phi}) + \left(Bh^2 - \frac{H^2}{3} \right) \nabla F_2(\tilde{\phi}) \right\} \\ & + \mu^4 H \left\{ \left[(A - 1) F_3(\tilde{\phi}) + 2 \left(Bh - \frac{H}{2} \right) F_4(\tilde{\phi}) + 3 \left(Ch^2 - \frac{H^2}{3} \right) F_5(\tilde{\phi}) \right. \right. \\ & \left. \left. + 4 \left(Dh^3 - \frac{H^3}{4} \right) F_6(\tilde{\phi}) \right] \nabla h + \left(Ah - \frac{H}{2} \right) \nabla F_3(\tilde{\phi}) \right. \\ & \left. + \left(Bh^2 - \frac{H^2}{3} \right) \nabla F_4(\tilde{\phi}) + \left(Ch^3 - \frac{H^3}{4} \right) \nabla F_5(\tilde{\phi}) + \left(Dh^4 - \frac{H^4}{5} \right) \nabla F_6(\tilde{\phi}) \right\} \end{aligned} \quad (29)$$

with $H = h + \delta\eta$. Substituting Eq. (22) into Eq. (5) and neglecting terms of $O(\mu^6)$ and higher, we obtain the approximate Bernoulli equation evaluated at $z = \delta\eta$

$$\begin{aligned} \eta + \tilde{\phi}_t + \mu^2 & \left[(Ah - H)F_1(\tilde{\phi}_t) + (Bh^2 - H^2)F_2(\tilde{\phi}_t) \right] + \mu^4 \left[(Ah - H)F_3(\tilde{\phi}_t) \right. \\ & \left. + (Bh^2 - H^2)F_4(\tilde{\phi}_t) + (Ch^3 - H^3)F_5(\phi_t) + (Dh^4 - H^4)F_6(\tilde{\phi}_t) \right] \\ & + \frac{\delta}{2} \left\{ |\nabla\tilde{\phi}|^2 + 2\nabla\tilde{\phi} \cdot \nabla \left[\mu^2 \{ (Ah - H)F_1(\tilde{\phi}) + (Bh^2 - H^2)F_2(\tilde{\phi}) \} \right. \right. \\ & \left. \left. + \mu^4 \{ (Ah - H)F_3(\tilde{\phi}) + (Bh^2 - H^2)F_4(\tilde{\phi}) + (Ch^3 - H^3)F_5(\tilde{\phi}) \right. \right. \\ & \left. \left. + (Dh^4 - H^4)F_6(\tilde{\phi}) \} + \mu^4 |\nabla \{ (Ah - H)F_1(\tilde{\phi}) + (Bh^2 - H^2)F_2(\tilde{\phi}) \}|^2 \right. \right. \\ & \left. \left. + \mu^2 [F_1(\tilde{\phi}) + 2F_2(\tilde{\phi})]^2 + 2\mu^4 [F_3(\tilde{\phi}) + 2HF_4(\tilde{\phi}) + 3H^2F_5(\tilde{\phi}) \right. \right. \\ & \left. \left. + 4H^3F_6(\tilde{\phi})] [F_1(\tilde{\phi}) + 2HF_2(\tilde{\phi})] \right\} = 0. \end{aligned} \tag{30}$$

The set of Eqs. (7), (29) and (30) form a fully nonlinear Boussinesq-type model based on a velocity potential $\tilde{\phi}$. We define a velocity vector

$$\tilde{\mathbf{u}}(x, y, t) = \beta [\nabla\phi]_{z=z_a} + (1 - \beta) [\nabla\phi]_{z=z_b}. \tag{31}$$

The relationship between $\tilde{\mathbf{u}}$ and $\tilde{\phi}$ can be found by inverting the gradient of Eq. (22) and substituting into Eq. (31), and is given by

$$\begin{aligned} \nabla\tilde{\phi} = \tilde{\mathbf{u}} - \mu^2 \nabla h & \left[(A - 1)F_{21} + 2(B - A)hF_{22} \right] - \mu^4 \nabla h \left[(A - 1)(F_{41} + F_{43}) \right. \\ & \left. + 2(B - A)h(F_{42} + F_{44}) + 3(C - B)h^2F_{45} + 4(D - C)h^3F_{46} \right], \end{aligned} \tag{32}$$

where

$$F_{21}(\tilde{\mathbf{u}}) \equiv G\nabla h \cdot \tilde{\mathbf{u}}, \tag{33}$$

$$F_{22}(\tilde{\mathbf{u}}) \equiv \frac{1}{2}G\nabla \cdot \tilde{\mathbf{u}}, \tag{34}$$

$$F_{41}(\tilde{\mathbf{u}}) \equiv -|\nabla h|^2 \left[(A - 1)\nabla h \cdot \tilde{\mathbf{u}} + (B - A)h\nabla \cdot \tilde{\mathbf{u}} \right], \tag{35}$$

$$F_{42}(\tilde{\mathbf{u}}) \equiv -\frac{1}{2}\nabla^2 h \left[(A - 1)\nabla h \cdot \tilde{\mathbf{u}} + (B - A)h\nabla \cdot \tilde{\mathbf{u}} \right], \tag{36}$$

$$F_{43}(\tilde{\mathbf{u}}) \equiv \nabla h \cdot \nabla (Ah\nabla h \cdot \tilde{\mathbf{u}}) + \frac{1}{2}\nabla h \cdot \nabla (Bh^2\nabla \cdot \tilde{\mathbf{u}}), \tag{37}$$

$$\begin{aligned} F_{44}(\tilde{\mathbf{u}}) \equiv \frac{1}{2}\nabla^2 (Ah\nabla h \cdot \tilde{\mathbf{u}}) + \frac{1}{4}\nabla^2 (Bh^2\nabla \cdot \tilde{\mathbf{u}}) \\ - \frac{1}{2}\nabla^2 h\nabla h \cdot \tilde{\mathbf{u}} - \nabla h \cdot \nabla (\nabla h \cdot \tilde{\mathbf{u}}), \end{aligned} \tag{38}$$

$$F_{45}(\tilde{\mathbf{u}}) \equiv -\frac{1}{6}\nabla^2 h\nabla \cdot \tilde{\mathbf{u}} - \frac{1}{3}\nabla h \cdot \nabla (\nabla \cdot \tilde{\mathbf{u}}) - \frac{1}{6}\nabla^2 (\nabla h \cdot \tilde{\mathbf{u}}), \tag{39}$$

$$F_{46}(\tilde{\mathbf{u}}) \equiv -\frac{1}{24}\nabla^2 (\nabla \cdot \tilde{\mathbf{u}}). \tag{40}$$

We then substitute Eq. (32) into the expression (29) for \mathbf{M} , and into the gradient of the Bernoulli Eq. (30). The resulting set of evolution equations are the approximate conservation laws using the velocity-type variable $\tilde{\mathbf{u}}$, and is given by Eq. (7) with

$$\begin{aligned} \mathbf{M} = H & \left\{ \tilde{\mathbf{u}} + \mu^2 \left[\left(Ah - \frac{H}{2} \right) (2\nabla hF_{22} + \nabla F_{21}) + \left(Bh^2 - \frac{H^2}{3} \right) \nabla F_{22} \right] \right. \\ & + \mu^4 \left[\left(Ah - \frac{H}{2} \right) (2\nabla hF_{42} + \nabla F_{41} + 2\nabla hF_{44} + \nabla F_{43}) \right. \\ & + \left(Bh^2 - \frac{H^2}{3} \right) (\nabla F_{42} + 3\nabla hF_{45} + \nabla F_{44}) \\ & \left. \left. + \left(Ch^3 - \frac{H^3}{4} \right) (4\nabla hF_{46} + \nabla F_{45}) + \left(Dh^4 - \frac{H^4}{5} \right) \nabla F_{46} \right] \right\}, \end{aligned} \quad (41)$$

for mass conservation, and

$$\mathbf{U}_t = -\nabla\eta - \frac{\delta}{2} \nabla(|\tilde{\mathbf{u}}|^2) + \Gamma_1(\eta, \tilde{\mathbf{u}}_t) + \Gamma_2(\eta, \tilde{\mathbf{u}}), \quad (42)$$

for momentum conservation. U , Γ_1 , and Γ_2 are given by

$$\begin{aligned} \mathbf{U} \equiv \tilde{\mathbf{u}} + \mu^2 & \left[(A-1)h(2\nabla hF_{22} + \nabla F_{21}) + (B-1)h^2\nabla F_{22} \right] \\ & + \mu^4 \left[(A-1)h(2\nabla hF_{42} + \nabla F_{41} + 2\nabla hF_{44} + \nabla F_{43}) \right. \\ & + (B-1)h^2(\nabla F_{42} + 3\nabla hF_{45} + \nabla F_{44}) + (C-1)h^3(4\nabla hF_{46} + \nabla F_{45}) \\ & \left. + (D-1)h^4\nabla F_{46} \right], \end{aligned} \quad (43)$$

$$\begin{aligned} \Gamma_1 \equiv \mu^2 \nabla & \left[\delta\eta F_{21t} + (2h\delta\eta + \delta^2\eta^2)F_{22t} \right] + \mu^4 \nabla \left[\delta\eta(F_{41t} + F_{43t}) \right. \\ & + (2h\delta\eta + \delta^2\eta^2)(F_{42t} + F_{44t}) + (3h^2\delta\eta + 3h\delta^2\eta^2 + \delta^3\eta^3)F_{45t} \\ & \left. + (4h^3\delta\eta + 6h^2\delta^2\eta^2 + 4h\delta^3\eta^3 + \delta^4\eta^4)F_{46t} \right], \end{aligned} \quad (44)$$

$$\begin{aligned} \Gamma_2 \equiv -\mu^2 \delta \nabla & \left\{ \tilde{\mathbf{u}} \cdot \left[(Ah - H)(\nabla F_{21} + 2\nabla hF_{22}) + (Bh^2 - H^2)\nabla F_{22} \right] \right. \\ & + \frac{1}{2} (F_{21} + 2HF_{22})^2 \left. \right\} - \mu^4 \delta \nabla \left\{ \tilde{\mathbf{u}} \cdot \left[(Ah - H)(\nabla F_{41} + 2\nabla hF_{42} + \nabla F_{43} \right. \right. \\ & + 2\nabla hF_{44}) + (Bh^2 - H^2)(\nabla F_{42} + \nabla F_{44} + 3\nabla hF_{45}) \\ & + (Ch^3 - H^3)(\nabla F_{45} + 4\nabla hF_{46}) + (Dh^4 - H^4)\nabla F_{46} \left. \right] \\ & + \frac{1}{2} \left[(Ah - H)(\nabla F_{21} + 2\nabla hF_{22}) + (Bh^2 - H^2)\nabla F_{42} \right]^2 \\ & \left. + \frac{1}{2} \left[(F_{21} + 2HF_{22})(F_{41} + 2HF_{42} + F_{43} + 2HF_{44} + 3H^2F_{45} + 4H^3F_{46}) \right] \right\}. \end{aligned} \quad (45)$$

Once $\tilde{\mathbf{u}}$ is known, the actual velocity field can be computed from substituting Eq. (32) into the gradient of Eq. (22).

The resulting model is referred to below as the fully-nonlinear fourth-order model, or FN4. To obtain a set of $O(\mu^4)$ weakly dispersive, weakly nonlinear equations with $\delta = O(\mu^2)$ (as in the standard Boussinesq approximation), terms of $O(\delta^2\mu^2)$ and smaller should be neglected. The resulting model is referred to below as the weakly-nonlinear fourth-order model or WN4. Finally, to recover the WKGS model, one must neglect terms of $O(\mu^4)$ while keeping all terms proportional to powers of δ , and set $\beta = 1$. Nwogu's parameter α_N is then related to A and B by

$$A = \sqrt{B}, \quad B = 2\alpha_N + 1 \quad (46)$$

with $\tilde{\mathbf{u}}$ being replaced by WKGS's \mathbf{u}_α .

In the following, we restrict our attention to a one-dimensional version in x , obtained by assuming $\tilde{\mathbf{u}} \equiv \tilde{u}$, and $\nabla \equiv \partial/\partial x$.

3. Numerical implementation

In this section we present the numerical implementation of the FN4 (and WN4) model derived in Section 2. The philosophy behind the numerical scheme follows very closely the one of WKGS, but extended to higher accuracy for consistency with the higher accuracy of the model itself. The time integration is done using a high order predictor–corrector scheme and the spatial derivatives are approximated with high order finite differencing. The order of accuracy in all the discretized terms in the equations is such that the truncation errors, which contain dispersive-type quantities, are always smaller than the highest-order dispersive term in the equations. This was done to assure that even when using relatively large grid spacing, the dispersion introduced by the error due to the discretization will not overwhelm the dispersive terms in the equations themselves. In WKGS, this is accomplished by making the truncation errors of $O(\mu^4)$ when combined with the term being discretized, assuming $k\Delta x = O(\mu)$. Since the present model contains $O(\mu^4)$ dispersion, more accuracy in the approximate derivatives is needed, so that the numerical truncation leads to errors of order higher than $O(\mu^4)$. Among the several ways to implement the boundary conditions, we choose to use fully reflective walls, with energy absorbing sponge layers used near the boundary in order to implement a radiation condition. With this kind of formulation, it is necessary to include some kind of wave generation inside the domain. The wave generation is implemented by introducing a source function in the mass conservation equation acting on a limited ‘source region’ conveniently placed in the domain.

We rewrite the one dimensional equations with the source function and the sponge layers as follows:

$$\eta_t = -M_x + f_s(x, t), \quad (47)$$

$$U_t = -\eta_x - \frac{\delta}{2}(\tilde{u}^2)_x + \Gamma_1(\eta, \tilde{u}_t) + \Gamma_2(\eta, \tilde{u}) - \tilde{u}f_d(x), \quad (48)$$

where M , U , Γ_1 , Γ_2 are the one-dimensional (in x) versions of the quantities defined in Eqs. (41), (43)–(45), and where $f_s(x, t)$ represents the source function and $\tilde{u}f_d(x)$ represents a dissipation term acting in the sponge layers. The sponge layer formulation used is given by Wei and Kirby (1995).

3.1. Discretization and solution method

We discretize the spatial coordinate x by: $x_i = i\Delta x$, ($i = 0, 1, 2, \dots, N$) and time t by: $t^j = j\Delta t$, ($j = 0, 1, 2, \dots, N_t$). There are three basic steps in advancing the solution by Δt in time: (i) the right-hand-sides of Eqs. (47) and (48) are evaluated, (ii) the equations are integrated in time to solved for η and U , (iii) \tilde{u} is evaluated from U . Since we use a predictor–corrector integration method and we have nonlinear terms containing time derivatives on the right-hand-side of Eq. (48), starting at the corrector stage of step (i), steps (i) through (iii) are iterated until convergence is attained. We present each of these steps in the following subsections.

3.1.1. Evaluation of the right-hand-sides

The finite-difference approximations to the spatial derivatives in the equations are done in such a way that the truncation error in each term of the equations should lead to errors of order higher than $O(\mu^4)$, assuming that $\Delta x = O(h_0)$ so that $k_0\Delta x = O(\mu)$. Notice that the momentum Eq. (48) contains first order time derivatives of \tilde{u} in Γ_1 . These time derivatives are evaluated in conjunction with the predictor–corrector iteration scheme (presented later) by using a finite difference approximation with values of \tilde{u} at times ($j, j-1, j-2, j-3, j-4$) Δt in the predictor stage and ($j+1, j, j-1, j-2, j-3, j-4$) Δt in the corrector stage. The formulas for the time derivatives at each of those j locations were obtained by expanding the variables in Taylor series around each j , multiplying each expansion by a coefficient and solving the system of equations resulting from setting the combination of coefficients of the higher derivatives of t to zero. The formulas are

$$\tilde{u}_i^{j-4} = \frac{1}{12\Delta t} \left(-3\tilde{u}_i^j + 16\tilde{u}_i^{j-1} - 36\tilde{u}_i^{j-2} + 48\tilde{u}_i^{j-3} - 25\tilde{u}_i^{j-4} \right) + O(\Delta t^4), \quad (49)$$

$$\tilde{u}_i^{j-3} = \frac{1}{12\Delta t} \left(\tilde{u}_i^j - 6\tilde{u}_i^{j-1} + 18\tilde{u}_i^{j-2} - 10\tilde{u}_i^{j-3} - 3\tilde{u}_i^{j-4} \right) + O(\Delta t^4), \quad (50)$$

$$\tilde{u}_i^{j-2} = \frac{1}{12\Delta t} \left(-\tilde{u}_i^j + 8\tilde{u}_i^{j-1} - 8\tilde{u}_i^{j-3} + \tilde{u}_i^{j-4} \right) + O(\Delta t^4), \quad (51)$$

$$\tilde{u}_i^{j-1} = \frac{1}{12\Delta t} \left(3\tilde{u}_i^j + 10\tilde{u}_i^{j-1} - 18\tilde{u}_i^{j-2} + 6\tilde{u}_i^{j-3} - 1\tilde{u}_i^{j-4} \right) + O(\Delta t^4), \quad (52)$$

$$\tilde{u}_i^j = \frac{1}{12\Delta t} \left(25\tilde{u}_i^j - 48\tilde{u}_i^{j-1} + 36\tilde{u}_i^{j-2} - 16\tilde{u}_i^{j-3} + 3\tilde{u}_i^{j-4} \right) + O(\Delta t^4), \quad (53)$$

for the predictor stage, and

$$\begin{aligned} \tilde{u}_i^{j-4} = & \frac{1}{60\Delta t} \left(12\tilde{u}_i^{j+1} - 75\tilde{u}_i^j + 200\tilde{u}_i^{j-1} - 300\tilde{u}_i^{j-2} + 300\tilde{u}_i^{j-3} - 137\tilde{u}_i^{j-4} \right) \\ & + O(\Delta t^5), \end{aligned} \quad (54)$$

$$\begin{aligned} \tilde{u}_i^{j-3} = & \frac{1}{60\Delta t} \left(-3\tilde{u}_i^{j+1} + 20\tilde{u}_i^j - 60\tilde{u}_i^{j-1} + 120\tilde{u}_i^{j-2} - 65\tilde{u}_i^{j-3} - 12\tilde{u}_i^{j-4} \right) \\ & + O(\Delta t^5), \end{aligned} \quad (55)$$

$$\begin{aligned} \tilde{u}_i^{j-2} = & \frac{1}{60\Delta t} \left(2\tilde{u}_i^{j+1} - 15\tilde{u}_i^j + 60\tilde{u}_i^{j-1} - 20\tilde{u}_i^{j-2} - 30\tilde{u}_i^{j-3} + 3\tilde{u}_i^{j-4} \right) \\ & + O(\Delta t^5), \end{aligned} \quad (56)$$

$$\begin{aligned} \tilde{u}_i^{j-1} = & \frac{1}{60\Delta t} \left(-3\tilde{u}_i^{j+1} + 30\tilde{u}_i^j + 20\tilde{u}_i^{j-1} - 60\tilde{u}_i^{j-2} + 15\tilde{u}_i^{j-3} - 2\tilde{u}_i^{j-4} \right) \\ & + O(\Delta t^5), \end{aligned} \quad (57)$$

$$\begin{aligned} \tilde{u}_i^j = & \frac{1}{60\Delta t} \left(12\tilde{u}_i^{j+1} + 65\tilde{u}_i^j - 120\tilde{u}_i^{j-1} + 60\tilde{u}_i^{j-2} - 20\tilde{u}_i^{j-3} + 3\tilde{u}_i^{j-4} \right) \\ & + O(\Delta t^5), \end{aligned} \quad (58)$$

$$\begin{aligned} \tilde{u}_i^{j+1} = & \frac{1}{60\Delta t} \left(137\tilde{u}_i^{j+1} - 300\tilde{u}_i^j + 300\tilde{u}_i^{j-1} - 200\tilde{u}_i^{j-2} + 75\tilde{u}_i^{j-3} - 12\tilde{u}_i^{j-4} \right) \\ & + O(\Delta t^5), \end{aligned} \quad (59)$$

for the corrector stage.

For Eq. (47) all but the boundary points (that is, $i = 1, \dots, N-1$) are evaluated. After the time integration is done (see Section 3.1.2), a boundary condition $\eta_x = 0$ is applied at $i = 0$ and $i = N$. A 7-point off-centered derivative of η is used and η_0^{j+1} and η_N^{j+1} can be obtained as:

$$\begin{aligned} \eta_{0,N}^{j+1} = & \frac{1}{147} \left(360\eta_{1,N-1}^{j+1} - 450\eta_{2,N-2}^{j+1} + 400\eta_{3,N-3}^{j+1} - 225\eta_{4,N-4}^{j+1} + 72\eta_{5,N-5}^{j+1} \right. \\ & \left. - 10\eta_{6,N-6}^{j+1} \right) + O(\Delta x^7). \end{aligned} \quad (60)$$

For Eq. (48), we only evaluate the terms at points $i = 2, \dots, N-2$. The remaining points do not need to be evaluated since at those points, the values of \tilde{u} are determined by boundary conditions. This is done when we evaluate \tilde{u} from U , defined in Eq. (43), and the procedure will be explained later.

The formulas for the spatial derivatives in Eqs. (47) and (48) are given in Appendix A.

3.1.2. Time integration

The integration method used is a 5th order predictor, 6th order corrector, Adams–Bashforth–Moulton scheme. Once the dependent variables are known at times $(j-4,$

$j - 3, j - 2, j - 1, j$) Δt , and the right-hand-sides of the equations have been evaluated, estimates of both η and U at time $(j + 1) \Delta t$ are made using the predictor step

$$v_{i_p}^{j+1} = v_i^j + \frac{\Delta t}{720} (1901V_i^j - 2774V_i^{j-1} + 2616V_i^{j-2} - 1274V_i^{j-3} + 251V_i^{j-4}) + O(\Delta t^6), \tag{61}$$

where index p stands for predictor. v_i^j is either U or η , and V_i^j is the right-hand-side of the respective equation, at $x = i\Delta x$ and $t = j\Delta t$. With the estimate U_p^{j+1} , we evaluate \tilde{u}_p^{j+1} (see Section 3.1.3) then estimate the right-hand-sides of the equations at t^{j+1} , $V_{i_p}^{j+1}$ and iterate the corrector stage where the predictor variables are the first estimates for the variables at iterative step k :

$$v_{i_{k+1}}^{j+1} = v_i^j + \frac{\Delta t}{1440} (475V_{i_k}^{j+1} + 1427V_i^j - 798V_i^{j-1} + 482V_i^{j-2} - 173V_i^{j-3} + 27V_i^{j-4}) + O(\Delta t^7), \tag{62}$$

until the error between $v_{i_{k+1}}^{j+1}$ and $v_{i_k}^{j+1}$ (where, again, v applies to both η and U) is small. We define an error estimate for the iteration process as:

$$E_{\text{iter}} = \left[\sum_{i=0}^N \frac{(\eta_{i_{k+1}}^{j+1} - \eta_{i_k}^{j+1})^2}{(\eta_{i_k}^{j+1})^2} \right]^{1/2} + \left[\sum_{i=0}^N \frac{(\tilde{u}_{i_{k+1}}^{j+1} - \tilde{u}_{i_k}^{j+1})^2}{(\tilde{u}_{i_k}^{j+1})^2} \right]^{1/2}, \tag{63}$$

and require that E_{iter} be smaller than an arbitrary tolerance T_{err} . In all our computations we used $10^{-9} < T_{\text{err}} < 10^{-12}$.

3.1.3. Evaluation of \tilde{u} from U

Once U has been evaluated at $t = (j + 1) \Delta t$ for $x = i\Delta x, i = 2, 3, \dots, N - 3, N - 2$, a system of algebraic equations can be written as

$$A_{m \cdot m} \tilde{u}_m = U_m, \quad m = N - 3, \tag{64}$$

where

$$A_{m \cdot m} = \begin{pmatrix} c_2 & d_2 & e_2 & 0 & \dots & 0 & 0 \\ b_3 & c_3 & d_3 & e_3 & \dots & 0 & 0 \\ a_4 & b_4 & c_4 & d_4 & e_4 & 0 & 0 \\ 0 & \dots & \dots & \dots & \dots & \dots & 0 \\ 0 & \dots & a_{N-4} & b_{N-4} & c_{N-4} & d_{N-4} & e_{N-4} \\ 0 & \dots & 0 & a_{N-3} & b_{N-3} & c_{N-3} & d_{N-3} \\ 0 & \dots & 0 & 0 & a_{N-2} & b_{N-2} & c_{N-2} \end{pmatrix}, \tag{65}$$

\tilde{u}_m and U_m are the vectors containing the unknowns \tilde{u} and U at $i = 2, \dots, N - 2$. Each row of the system represents the finite difference approximation for the definition of $U(\tilde{u})$. a_i, b_i, c_i, d_i, e_i are the coefficients appearing in front of \tilde{u} after the 5-point derivatives are substituted into Eq. (43), except for rows 2, 3, $N - 3, N - 2$, where these coefficients are modified to accommodate the boundary conditions given by $\tilde{u}_{,xx} = \tilde{u} = 0$.

After solving the system for \tilde{u} at $i = 2, \dots, N - 2$, we use these conditions (with an off-centered 5-point finite-difference approximation) to obtain

$$\tilde{u}_{0,N}^{j+1} = 0, \tag{66}$$

$$\tilde{u}_{1,N-1}^{j+1} = \frac{1}{104} (114\tilde{u}_{2,N-2}^{j+1} - 56\tilde{u}_{3,N-3}^{j+1} + 11\tilde{u}_{4,N-4}^{j+1}). \tag{67}$$

The justification for using the boundary conditions $\tilde{u}_{xx} = \tilde{u} = \eta_x = 0$ is to guarantee that the mass flux

$$M = h \left[\tilde{u} + \frac{1}{2} \left(B - \frac{1}{3} \right) h^2 \tilde{u}_{xx} + \frac{1}{4} \left(B^2 - \frac{B}{3} - \frac{D}{6} + \frac{1}{30} \right) h^4 \tilde{u}_{xxxx} \right], \tag{68}$$

vanishes at the walls, which can be verified exactly by substituting $\tilde{u}_{xx} = \tilde{u} = \eta_x = 0$ into the linearized flat bottom momentum equation:

$$g\eta_x + \left[\tilde{u} + \frac{1}{2} (B - 1) h^2 \tilde{u}_{xx} + \frac{1}{4} \left(B^2 - B - \frac{D}{6} + \frac{1}{6} \right) h^4 \tilde{u}_{xxxx} \right]_t = 0, \tag{69}$$

and obtaining that $\tilde{u}_{xxxx} = 0$, and therefore that $M = 0$ at the boundary.

3.1.4. Convergence and stability

No stability analysis for the present numerical formulation of the FN4 model was done, due to the complexity of the model as well as the numerical scheme. To attain the desired accuracy in the model with relatively fast convergence, the Courant number used in all cases was never larger than 0.3. The numerical implementation for the linearized model proved to be stable for all cases tested. For some cases, it was necessary to filter the solution as high frequency oscillations appeared near points where the bottom slope was discontinuous. This is due to the fact that the FN4 model contains terms proportional to high (up to fourth) derivatives of h with respect to x , and, for discontinuous bottom slopes, these factors become singular and can introduce spurious high frequency waves to the solution. When necessary we used a Shapiro (1970) filter with either nine or 17-point (Shapiro’s $n = 4$ and 8, respectively) average, and the filter was applied every N_f time steps where $50 < N_f < 500$, depending on the case. Ideally, as the number of points used in the average tends to infinity, this filter only affects the Nyquist frequency. In practice, for the cases studied, we verified that our use of the filter did not affect the solutions in any significant way, except to remove extremely high frequency noise.

In most cases where nonlinear effects become important (very steep, high waves), the iteration process tends to become slow, or even to diverge. To correct this problem we adopted a relaxation technique in the iteration process, as follows: if with two iterations the error tolerance is not met, we assume that the corrector is overshooting the desired solution and apply the following formula to both \tilde{u} and η :

$$f_{i_r}^{j+1} = (1 - R) f_{i_k}^{j+1} + R f_{i_{k+1}}^{j+1}, \tag{70}$$

where the relaxation coefficient R ranges from 0 to 1. $f_{i_k}^{j+1}$ is the estimate in the previous iteration, and $f_{i_{k+1}}^{j+1}$ is the estimate in the current iteration, which is replaced by the relaxed values $f_{i_r}^{j+1}$. The optimal value of R strongly depends the type of problem. For all the cases studied in this paper, we used $0.2 < R < 1$. The number of iterations necessary for convergence within the desired accuracy was typically between 1 and 6.

3.2. Source function for wave generation inside the domain

Using sponge layers near the boundaries rules out the possibility of any type of wave generation at the boundary. It is therefore necessary to introduce a source term inside the domain to generate the desired waves, which will propagate towards the boundaries, and be damped at the sponge layers. This is the role of the last term in Eq. (47), $f_s(x, t)$. The first attempt to include such terms in Boussinesq models was made by Larsen and Dancy (1983), in which mass is added and subtracted from the domain along a single line (or point, in the case of a one-dimensional model). Wei (1997) found that this approach, which worked well with the staggered grid of Larsen and Dancy (1983), did not work well in his non-staggered grid, where spurious noise appeared around the source point. It was necessary therefore to distribute the source function around a certain neighborhood of the source. In the present formulation, we closely follow the approach of Wei et al. (1999), in which the source function is assumed to be distributed as a Gaussian shape, making the appropriate modifications to account for the added complexity of the model. The formulation for the source function presented next is one-dimensional, but can be extended to two dimensions in a straightforward manner.

If the local water depth at the source region is constant, h , and we want to generate regular waves with angular frequency ω , the source function can be written as

$$f_s(x, t) = D_s \exp\left[-\beta_s(x - x_s)^2\right] \sin(\omega t), \quad (71)$$

where x_s is the center of source function, β_s determines how focused the source function is, and D_s is the magnitude of the source function. Assuming that the generated wave has small amplitude, we can use the linearized version of the FN4 model and derive an analytical expression for D_s using Green's functions (see Appendix B), to obtain

$$D_s = \frac{i\eta_0}{\omega A_G I_1 \left[1 + C_3(kh)^2 + C_4(kh)^4\right]}, \quad (72)$$

where k is the model wave number and C_3 , C_4 , A_G and I_1 are given in Appendix B.

Although the Gaussian shape parameter β_s is arbitrary, in practice its value has great influence on how well the source function can generate the desired waves. Ideally, β_s should be as large as possible, so that the source function would be more localized. However, it turns out that if the source region is too narrow (large β_s), the waves generated can be quite distorted and noise may also appear when they have finite amplitudes. Defining the width of the source region W_s to be the distance between two

coordinates (equidistant from the source center) where $\exp[-\beta_s(x-x_s)^2]$ is equal to e^{-5} , we can write

$$W_s = 2\sqrt{5/\beta_s}. \quad (73)$$

By trial and error, it was found that, for regular waves, a source with width W_s approximately equal to the wave length gives satisfactory results for waves within a wide range of amplitudes and wavenumbers. When the incident wave nonlinearity is very high ($O(1)$) the source function method fails to generate the waves properly. Sensitivity tests for W_s using several wave amplitudes were performed and yielded results which are similar to those shown of Wei et al. (1999). Results of these tests may be found in (Gobbi, 1998).

4. Comparisons with laboratory measurements

It is well known that regular waves decompose into higher frequency free waves as they propagate past a submerged bar, as shown in experimental work by Beji and Battjes (1993), Luth et al. (1994), and Ohyama et al. (1994). The basic mechanism is as follows: as the waves propagate onto the front slope of the bar, nonlinear interactions transfer energy from the leading wave component to higher harmonics, causing the wave to become steeper. The waves take on a negatively asymmetric, pitched-forward shape, which is a direct signature of the rapid transfer of energy to higher harmonics. After the peak of the bar is reached and the bottom slope becomes negative, the nonlinear coupling of the higher harmonics with the fundamental wave becomes progressively weaker, and, from higher to lower harmonics, each of the Fourier components are released as free waves with their own bound higher harmonics. Of course, since the waves after the bar travel with different speeds, the process can be fairly complicated. It is clear therefore that wave propagation over a submerged bar is a quite demanding test for Boussinesq-type models, as it requires that the model predict the nonlinear harmonic generation well, and also that the released shorter waves behind the bar have an accurate speed, which may not happen even if the model predicts well the speed of the primary waves before they reach the bar.

Comparisons between several weakly nonlinear Boussinesq-type models and experimental data by Beji and Battjes (1993) and Luth et al. (1994) of waves propagating over a submerged bar were presented by Dingemans (1994). In general, the models performed relatively well for the longer, lower amplitude waves, but all were fairly inaccurate for the shorter, more nonlinear waves, especially behind the bar.

Comparisons between the extended Boussinesq model of Nwogu (1993) and experimental data, also for waves passing over a submerged bar, were presented by Ohyama et al. (1994), and the results were similar to the comparisons made by Dingemans (1994); that is, the model poorly predicted waves behind the shoal for the shorter, higher wave cases.

In this section, we compare the FN4 model with two laboratory experimental data sets of regular waves propagating in a one-dimensional wave flume and over a

submerged bar: Luth et al. (1994), and Ohyama et al. (1994). We also show comparisons of the WKGS model with the same data sets. The models' comparisons with the data are done in three different manners: plots of free surface time series at fixed locations, spatial plots of Fourier components of the time series, and a quantitative estimation of accuracy defined by:

$$d_i = 1 - \frac{\sum_{j=n_1}^{n_2} [y(j) - y_d(j)]^2}{\sum_{j=n_1}^{n_2} [|y(j) - \bar{y}_d| + |y_d(j) - \bar{y}_d|]^2}, \tag{74}$$

where d_i is an index of agreement proposed by Wilmott (1981) for the i th wave gauge, and where n_1 and n_2 cover a full wave period in the time series.

$y_d(j)$ are the measured data to be compared with, $y(j)$ are the predicted values from the model, and \bar{y}_d is the mean value of $y_d(j)$. A perfect agreement between data and model corresponds to $d_i = 1$, while a complete disagreement results in $d_i = 0$. In all the numerical simulations we used $\Delta x = 0.025$ m and kept the Courant number below 0.3. The sponge layer strength and width used were $S = 30$ and $x_L - x_S = 3 L$, respectively. The width of the source function used was $W_s = L$, where L is the incident wave length. The details of the experiments and comparisons with the models are presented in the sections below.

4.1. The Delft Hydraulics experiments

The experiments performed by Beji and Battjes (1993) and Luth et al. (1994) have the same geometric characteristics, except for the length scale in (Luth et al., 1994), which is twice as large as in (Beji and Battjes, 1993). In Luth et al. (1994) all gauge locations used in (Beji and Battjes, 1993) were repeated, and another run of measurements was performed with the gauges at different locations. For the sake of consistency with the study by Dingemans (1994), we re-scale all measurements to the scales used in (Beji and Battjes, 1993). The layout of the experimental set-up with the locations of the measurement stations (to which we refer by their location, e.g., gauge 2.0 m, gauge 15.7 m, etc.) and the geometry of the flume are illustrated in Fig. 1. In the present work we

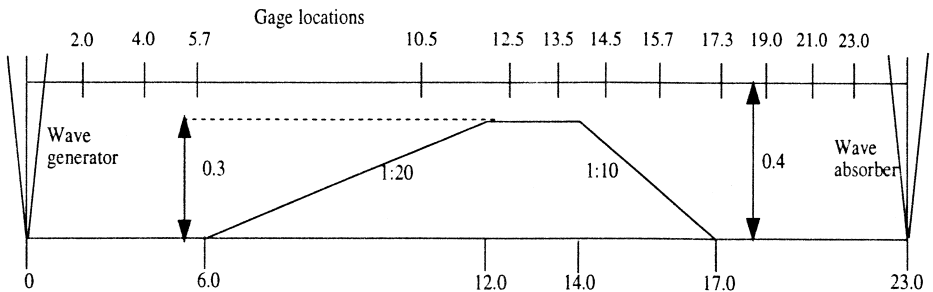


Fig. 1. Sketch of wave flume of Delft experiments. All dimensions in (m).

use the data from Luth et al. (1994), since in that experiment active wave absorption was used at the end of the flume and both reflection and bound long waves were monitored during the experiment.

Three sets of data were collected using different incident wave conditions. We refer to these data sets as cases (a), (b), and (c). In case (b), wave breaking occurred on the crest of the shoal, and therefore these data were disregarded, since the present model does not include any breaking mechanism. It is worthy mentioning an important point about the data set (c). For this case, the available data did not cover the entire time range which would ensure a permanent form periodic wave behind the shoal (only the first 46 s of data were provided). We, therefore, show comparisons between the data and the models' calculations at approximately the same time window in relation to the first waves in the time series; that is, for this case, we do not wait for the model to reach a periodic solution behind the bar. Of course this is not a straightforward task, since the model generates incident waves inside the domain in a peculiar manner, and the transient at the very start of the wave generation process can be quite different from that of a wave paddle.

The incident wave characteristics for cases (a) and (c) are given in Table 1. In all cases, the data from gauges at 2.0 m or 4.0 m (remember these are two experiments combined) were used to synchronize the data with the models.

Figs. 2 and 3 show comparisons with data from the Delft experiments for case (a) of the models WKGS and FN4. Notice that at station 5.7 m, there is a phase mismatch in the data. This systematic error is because the gauge is actually at a different location (5.2 m) than that provided with the data and for which the computations were done. We, however, preferred not to alter the original information and leave this as a note. Also, no data was available for station 23.0 m. Both the FN4 and WKGS models perform quite well for all the gauges up to the crest of the bar, but as the waves pass the back slope of the bar, the WKGS model shows some discrepancies with the data. This is due to the aforementioned decoupling of the higher harmonics from the primary longer wave which are released as free waves propagating with a larger value of μ which are more susceptible to inaccuracies. The FN4 model remains quite accurate even for the gauges located after the bar. To illustrate the inaccuracies due to higher harmonic decoupling, Fig. 4 shows a representation of the linear dispersion relationship where the nondimensional wave speed is plotted against the wave frequency. The vertical dotted lines indicate the location of the frequency of the fundamental wave in case (a), of which the period is $T_1 = 2.02$ s, and its harmonics with periods $T_2 = T_1/2$, $T_3 = T_1/3$, etc. Notice

Table 1
Incident wave characteristics for the Delft experiments

	Case (a)	Case (c)
Wave amplitude (m)	0.01	0.0205
Wave period (s)	2.02	1.01
$\mu \equiv k_0 h_0$	0.67	1.69
$\delta \equiv a_0 / h_0$	0.025	0.051

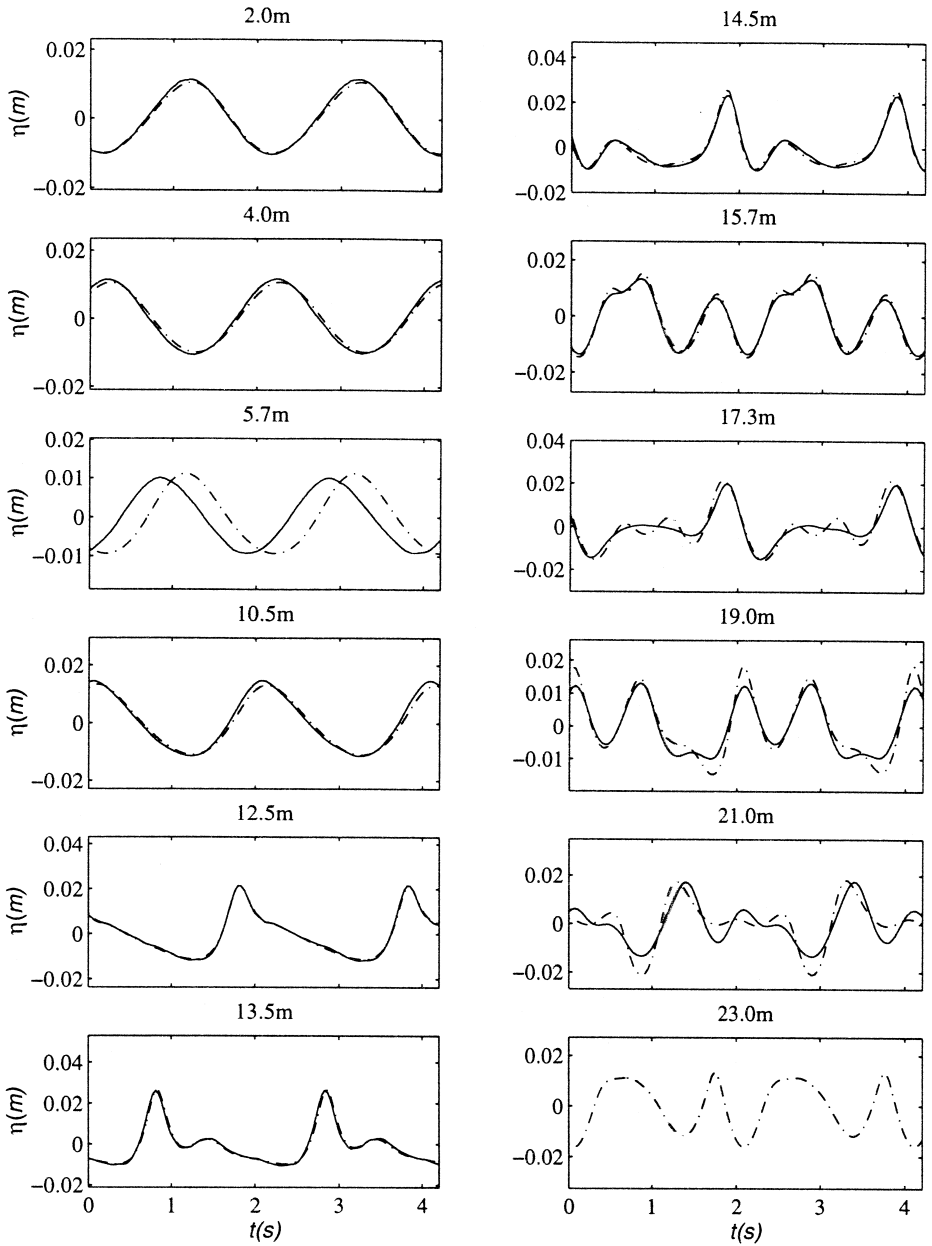


Fig. 2. Comparisons of free surface displacement with case (a) of Delft experimental data at several gauge locations. WKGS (dash-dot), data (solid).

that the phase speed error in the primary wave (T_1) is small for both the FN4 and WKGS models. As the bound waves are released as free waves they travel with their

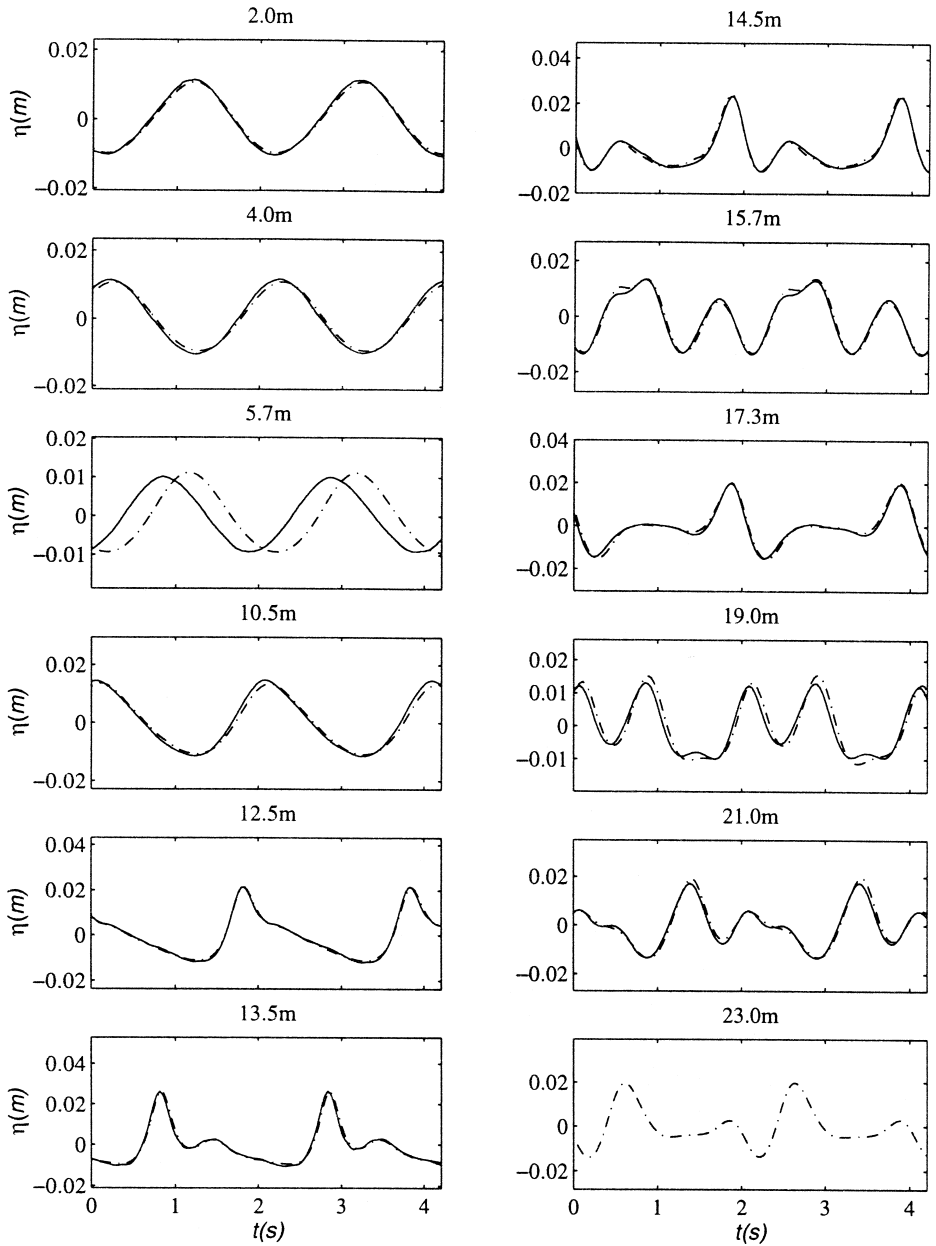


Fig. 3. Comparisons of free surface displacement with case (a) of Delft experimental data at several gauge locations. FN4 (dash-dot), data (solid).

own speed, which, in the linear limit, are represented by the intersection of the vertical lines T_2 , T_3 , etc., with each model's dispersion curve. Notice that the errors in the speed

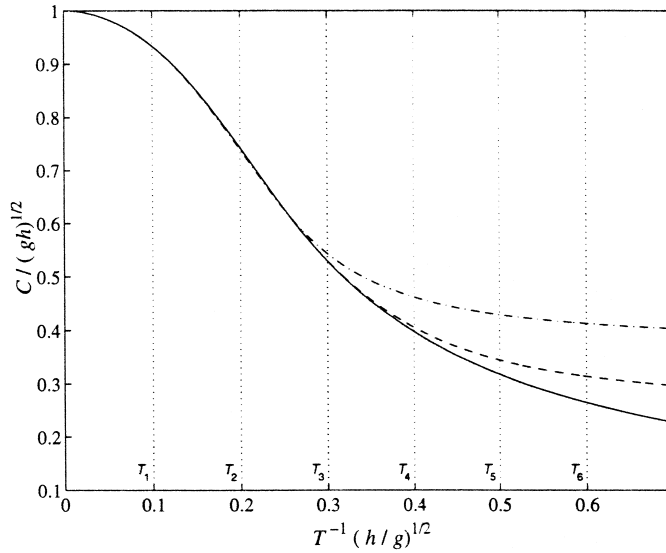


Fig. 4. Linear dispersion relationship as (nondimensional) wave speed vs. wave frequency. Present Model (dash), WKGS (dash-dot), exact (solid). Dotted vertical lines are waves with periods $T_n = (2.02/n)s$.

of the released higher harmonics starting from T_3 for WKGS are considerably larger than for the FN4 model.

Similarly to Figs. 2, 3, Figs. 5 shows plots for the WN4 model (the present model with the assumption $\delta = O(\mu^2)$ and neglecting terms of $O(\delta^2\mu^2, \delta\mu^4, \dots)$). Apart from slight phase differences, the comparison is about as good as for the FN4 model, which indicates that for this case, the improvement in the dispersion effects of the FN4 and WN4 models over the WKGS model is more important than the fully nonlinear effects accounted for in WKGS and FN4, but not in WN4.

Figs. 6–8 are analogous to Figs. 2, 3 and 5, but for case (c) (see Table 1). Firstly, we do not know how much the aforementioned transient problem in case (c) affected the comparisons shown below. In this case the incident wave has twice the amplitude and about 2/5 of the wavelength of case (a). Before the waves reach the back slope of the bar, FN4 and WKGS perform quite similarly, although some phase differences are apparent. Model WN4 does not perform as well in this case due to its weak nonlinearity assumption. As the waves pass over the bar, the higher harmonic decomposition combined with nonlinear effects are strong enough in this case to make the three models give very different results, with FN4 being the most accurate, giving very good agreement except for slight phase differences. WN4 also performs qualitatively worse than the WKGS (accurate to $O(\mu^2)$, but fully nonlinear) for all gauges up to 15.7 m. This result is a strong indication that the improvement in linear dispersion is not always more important than the fully nonlinear effects, contrary to the generalizing conclusion of Dingemans (1994). Referring back to Fig. 4, again, after the waves pass the bar, the higher harmonics are released as free waves. For case (c) the primary (incident) wave is indicated by the vertical dotted line labeled T_2 , and its second and third harmonics are

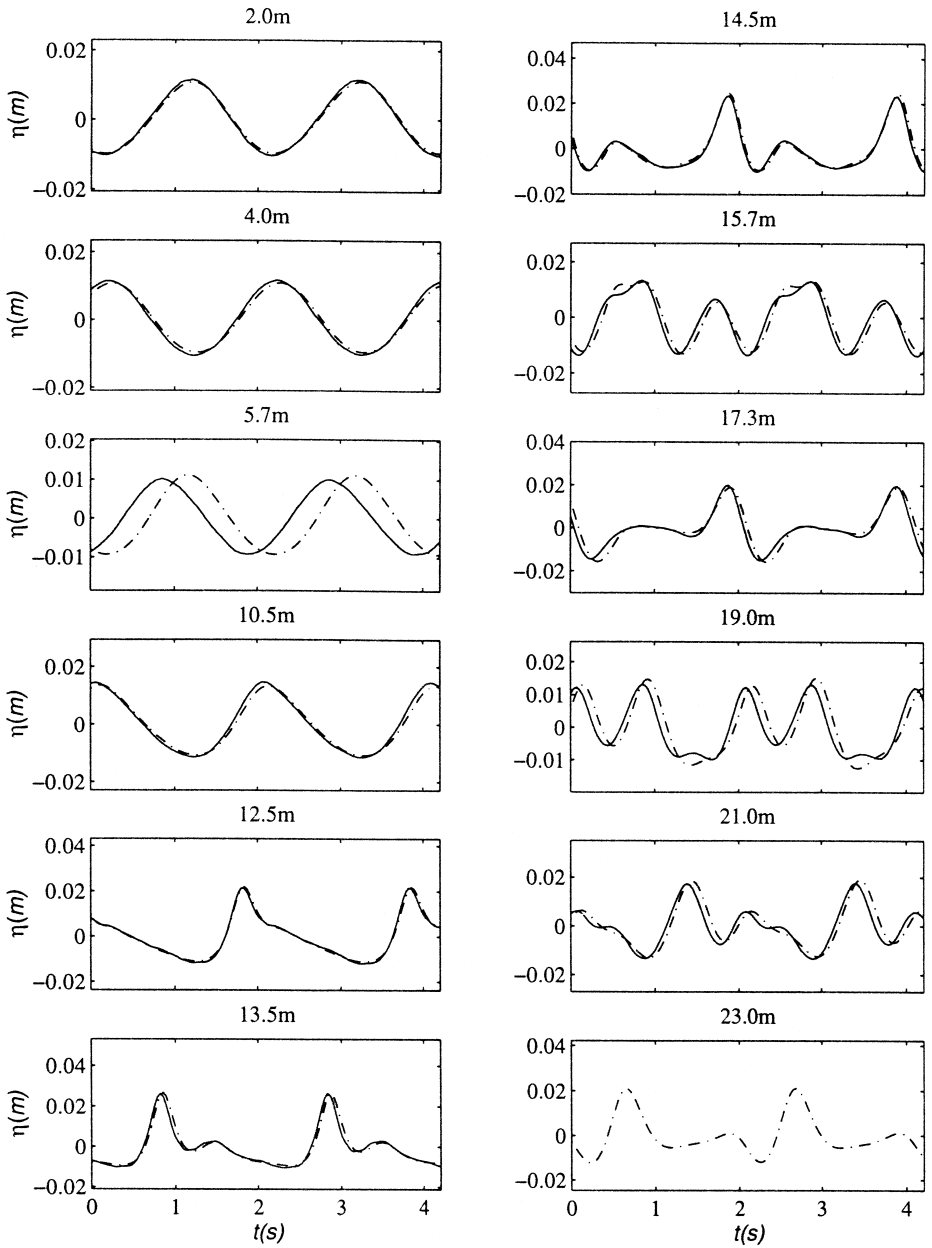


Fig. 5. Comparisons of free surface displacement with case (a) of Delft experimental data at several gauge locations. WN4 (dash-dot), data (solid).

represented by the even indexes, that is, T_4 and T_6 , respectively. Notice that the error in the speed of the primary wave is negligible for the WKGS model. In the second

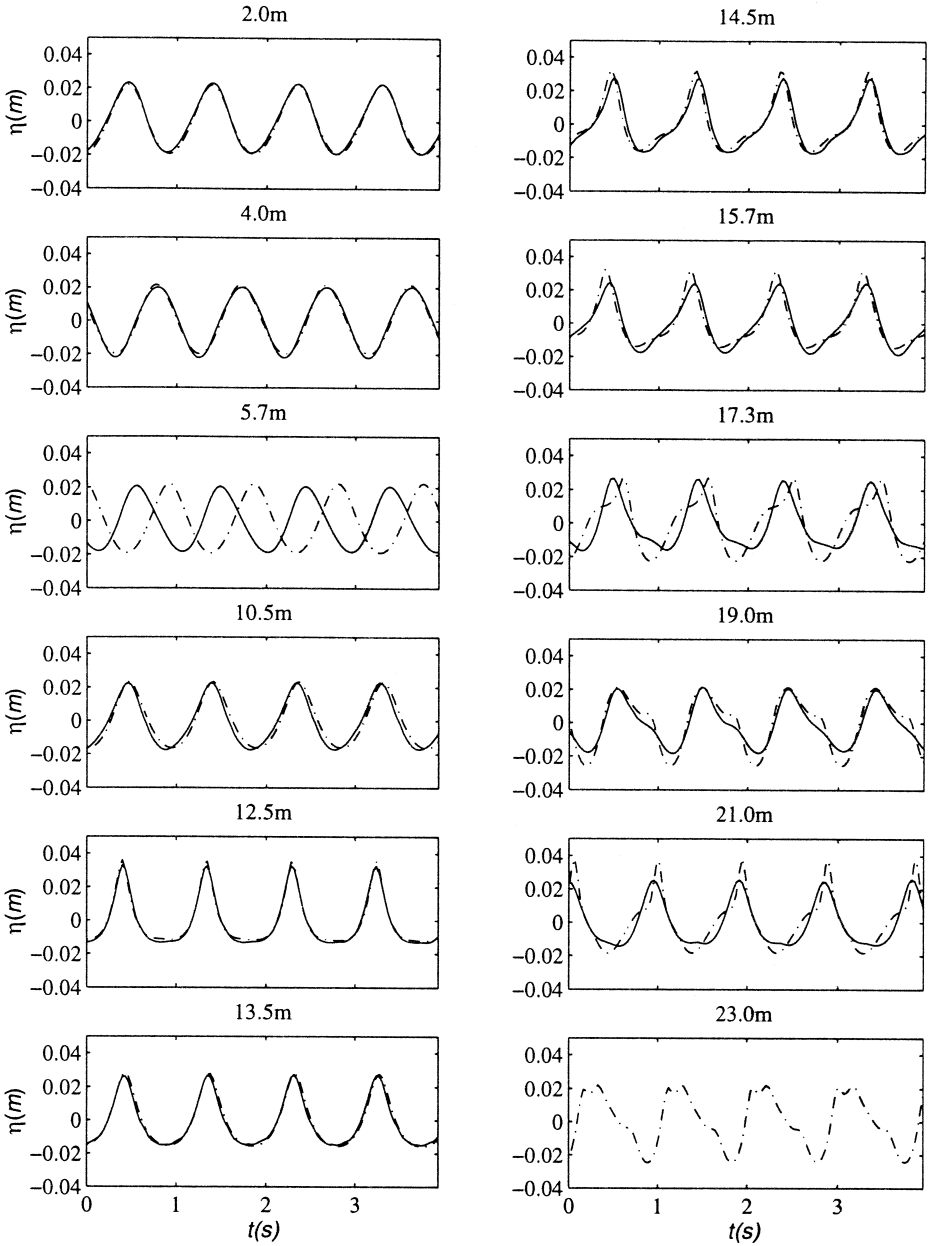


Fig. 6. Comparisons of free surface displacement with case (c) of Delft experimental data at several gauge locations. WKGS (dash-dot), data (solid).

harmonic (T_4) the error for WKGS is fairly high, and for FN4, although not negligible, is considerably smaller, and the same being the case of the released third harmonic (T_6).

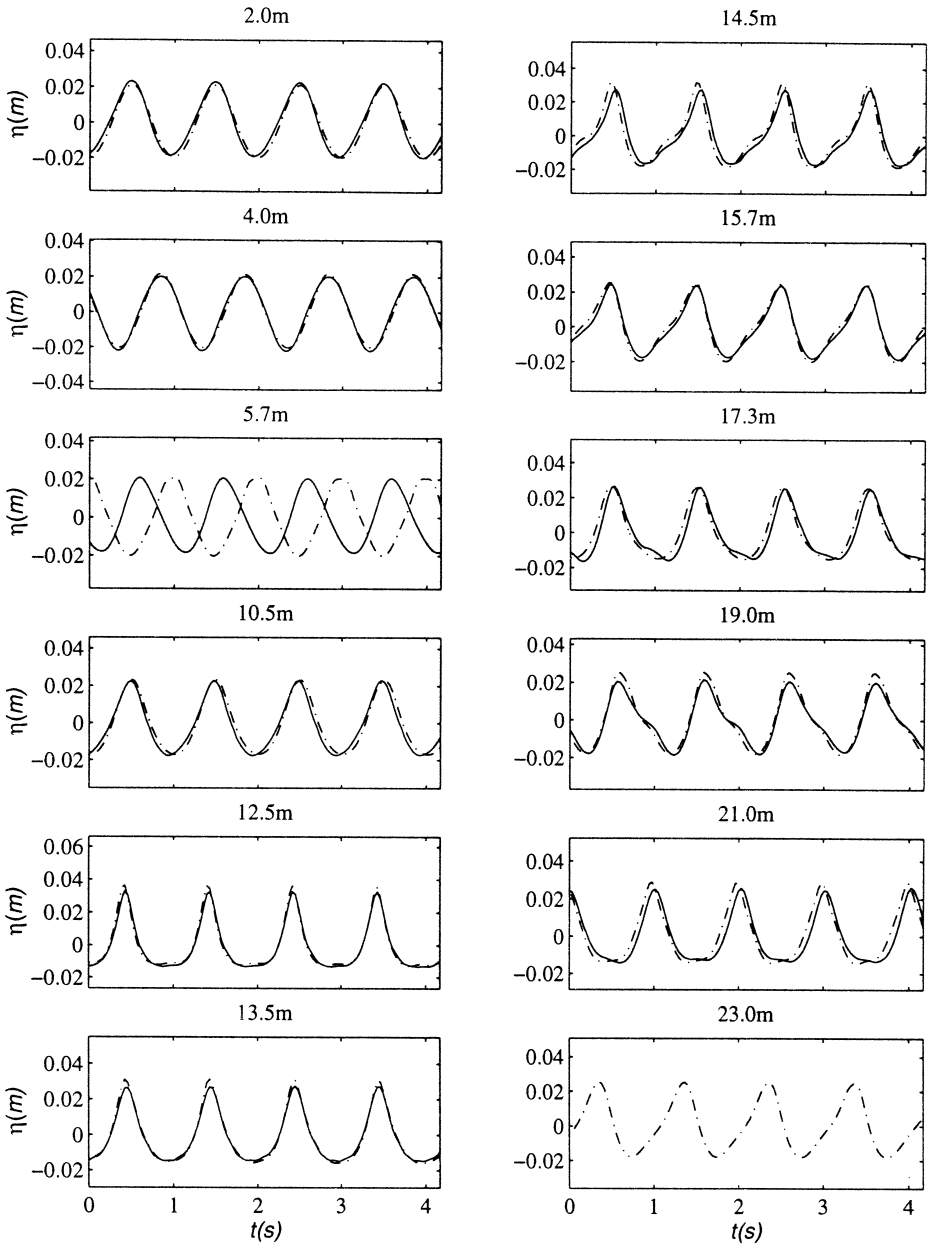


Fig. 7. Comparisons of free surface displacement with case (c) of Delft experimental data at several gauge locations. FN4 (dash-dot), data (solid).

Fig. 9 shows comparisons of the absolute value of the amplitudes of the Fourier transform of one wave period of the time series, between both FN4 and WKGS, and the

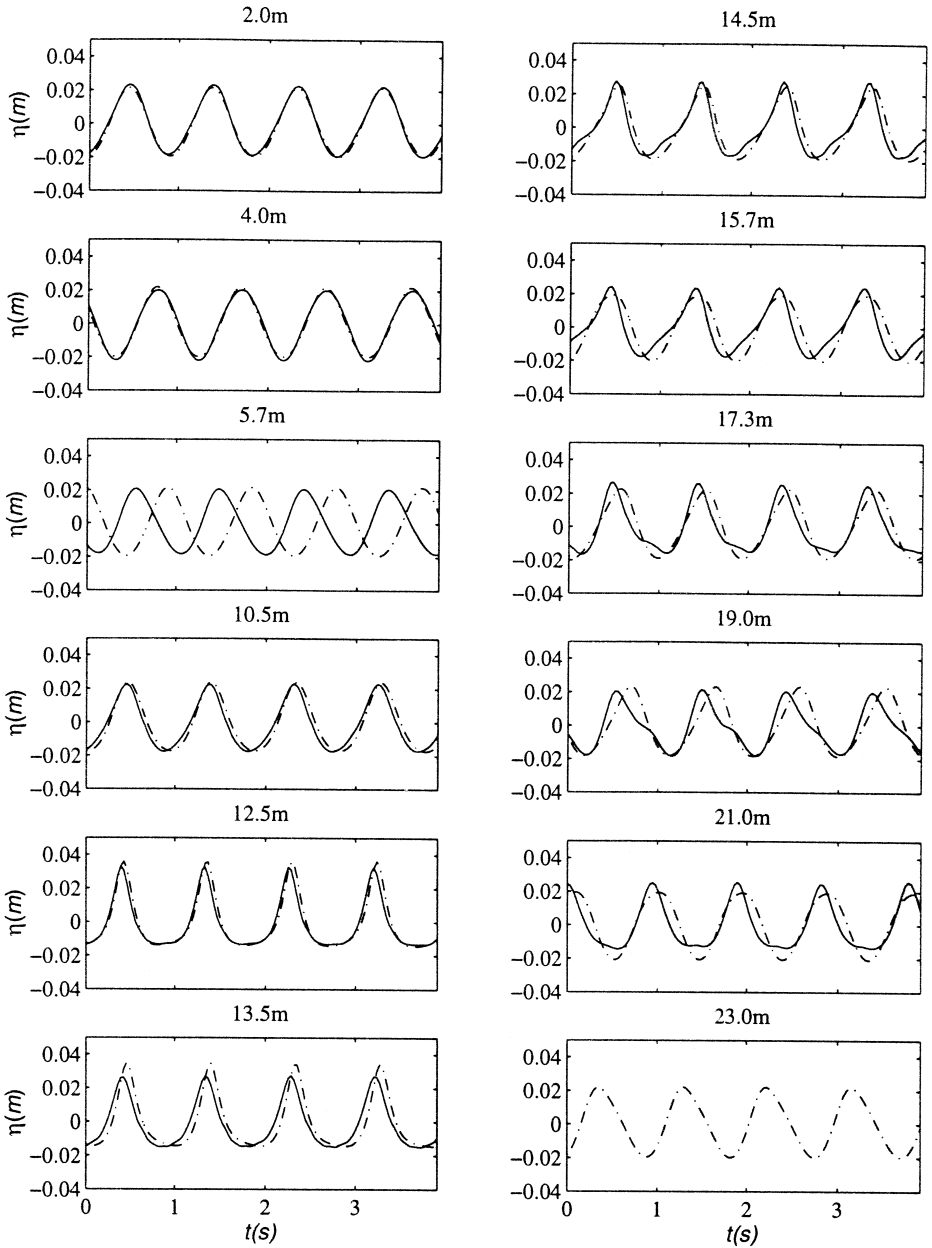


Fig. 8. Comparisons of free surface displacement with case (c) of Delft experimental data at several gauge locations. WN4 (dash-dot), data (solid).

data points at each gauge location for both cases (a) and (c). Fig. 10 shows similar plots for FN4 and WN4, where FN4 results are identical to those in Fig. 9. Also shown are

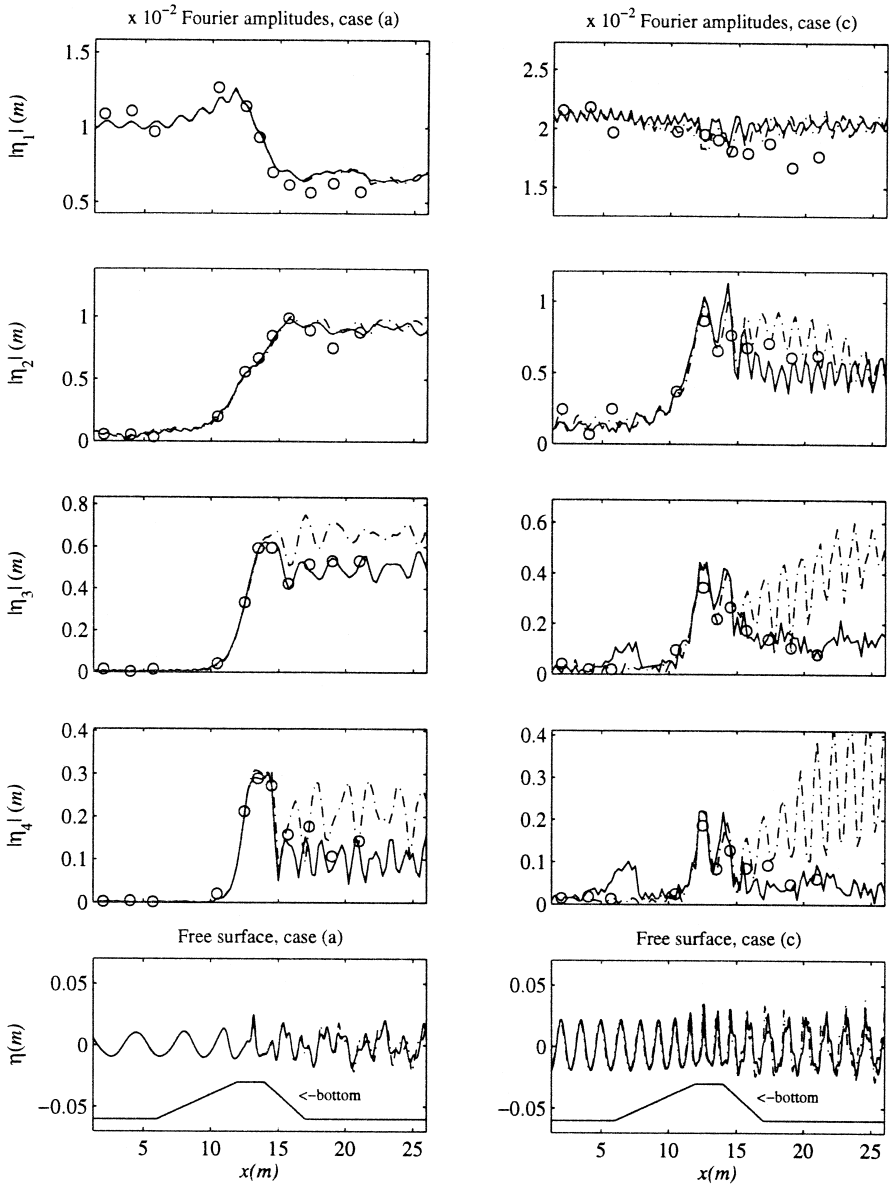


Fig. 9. Comparisons of the spatial variation of the Fourier components of the free surface displacement with cases (a) and (c) of Delft experimental data. Bottom panels show the free surface elevation. FN4 (solid), WKGS (dash-dot), data (circles).

snapshots of the free surface elevation and the position of the bar (out of scale). In both cases (a) and (c), the WKGS model tends to overpredict the higher harmonics after the crest of the bar. For case (a) the FN4 and WN4 models give very similar results, with

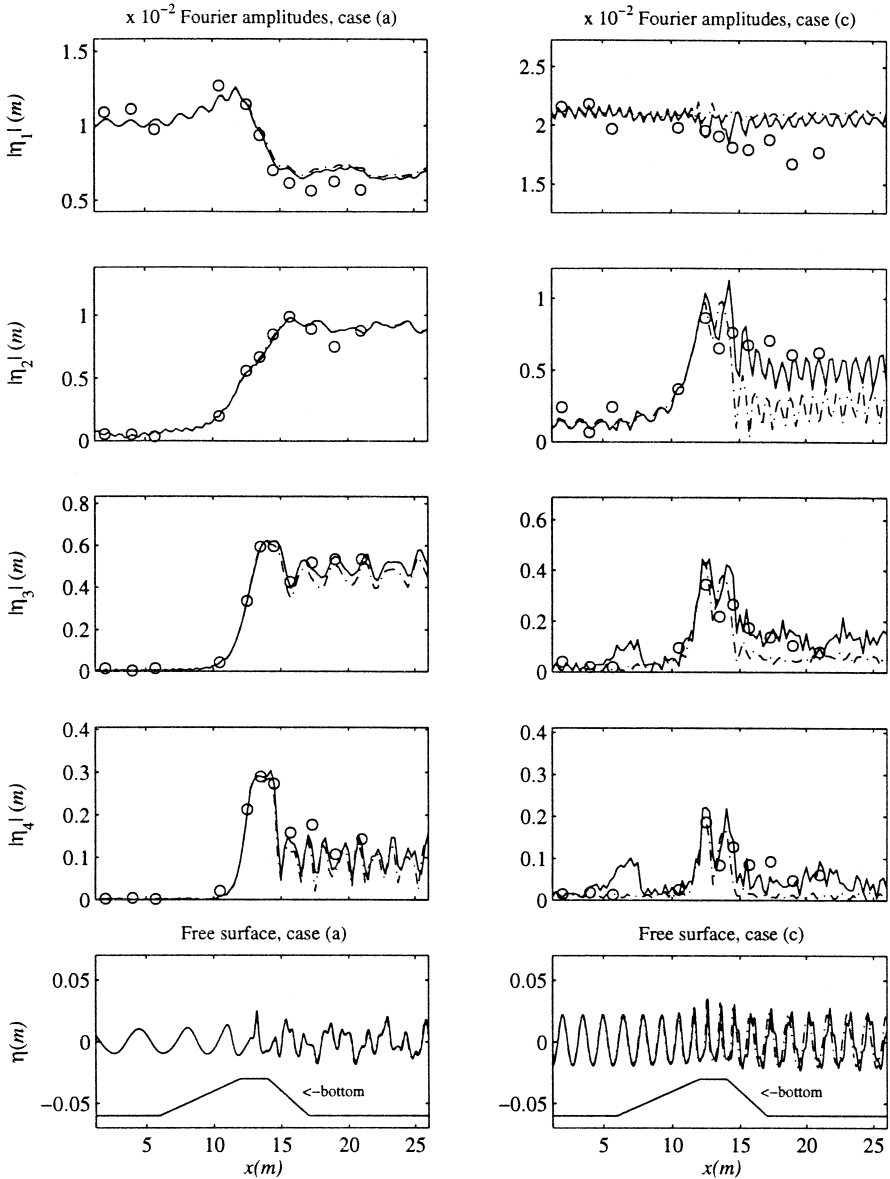


Fig. 10. Comparisons of the spatial variation of the Fourier components of the free surface displacement with cases (a) and (c) of Delft experimental data. Bottom panels show the free surface elevation. FN4 (solid), WN4 (dash-dot), data (circles).

some slight underpredictions by WN4 of the amplitudes of the released third and fourth harmonics after the bar crest. In case (c), WN4’s inability to generate higher harmonics accurately due to the weak nonlinearity assumption is evident in the underprediction of

Table 2
Index of agreement d_i

Gauge location (m)	Case (a)			Case (c)		
	WKGS	FN4	WN4	WKGS	FN4	WN4
2.0	0.998	0.998	0.998	0.997	0.996	0.998
4.0	0.996	0.996	0.996	0.997	0.997	0.984
10.5	0.995	0.995	0.995	0.982	0.986	0.997
12.5	0.999	0.999	0.998	0.997	0.995	0.927
13.5	0.996	0.995	0.987	0.996	0.996	0.990
14.5	0.995	0.997	0.993	0.979	0.971	0.883
15.7	0.995	0.996	0.980	0.973	0.993	0.977
17.3	0.975	0.995	0.972	0.880	0.973	0.934
19.0	0.973	0.982	0.943	0.968	0.987	0.970
21.0	0.927	0.993	0.962	0.948	0.965	0.931

the decomposed higher harmonics. Notice the modulation present in the fundamental wave before the bar, shown by all three models, caused by partial wave reflection from the front of the bar. Notice also that for case (c) the FN4 model slightly overpredicts the third and fourth modes around the toe of the front face of the bar. This is due to numerical error introduced by the high order derivative terms, which are undefined functions at that location. When necessary, the solution was filtered (see Section 4) to avoid high frequency contamination problems. In general, as in the case of the time series plots, the FN4 agrees with the data much better than WKGS and than WN4 for case (c).

Table 2 shows the index of agreement d_i , defined by Eq. (74) of the models FN4, WN4, and WKGS, with both cases (a) and (c) of the Delft experiments for all gauges except 5.7 m and 23.0 m. Of course, the differences in d_i between the models should only have significance when they are larger than d_i for the incident wave (gauges 2.0 m and 4.0 m). The results confirm that the best performance is from the FN4 model, with only one case where WKGS gave a slightly better result (case (c), gauge 14.5 m) due to a slightly larger phase mismatch in FN4. It is clear that the WKGS model outperforms the WN4 model around the bar crest (gauges 12.5 m through 14.5 m), but as the waves reach deeper water (importance of nonlinearity and dispersion switch), WKGS loses accuracy. Although WN4 has much more accurate dispersion relationship in deeper

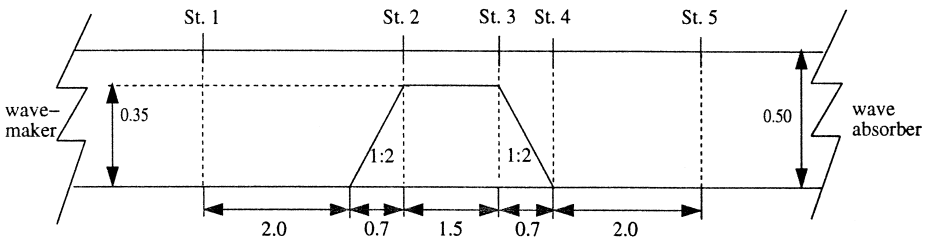


Fig. 11. Sketch of wave flume of the Ohyama experiment. All dimensions in (m).

Table 3
Incident wave characteristics for the Ohyama experiment

	Case (2)	Case (4)	Case (6)
Wave amplitude (m)	0.025	0.025	0.025
Wave period (s)	1.341	2.012	2.683
$\mu \equiv kh$	1.299	0.769	0.555
$\delta \equiv a_0 / h_0$	0.050	0.050	0.050

water than WKGS, since it was not capable of generating higher harmonics properly while the waves were shoaling, the overall solution becomes inaccurate after the bar. This confirms the importance of the full-nonlinearity assumption made in the WKGS derivation but not in the WN4.

4.2. The Ohyama experiment

In this section, we show comparisons between the FN4 and WKGS models with the experiment by Ohyama et al. (1994) (referred here as simply the Ohyama experiment). Computations with the WN4 model were not performed for this case. A sketch of the wave flume with the gauge locations is shown in Fig. 11. We now summarize the

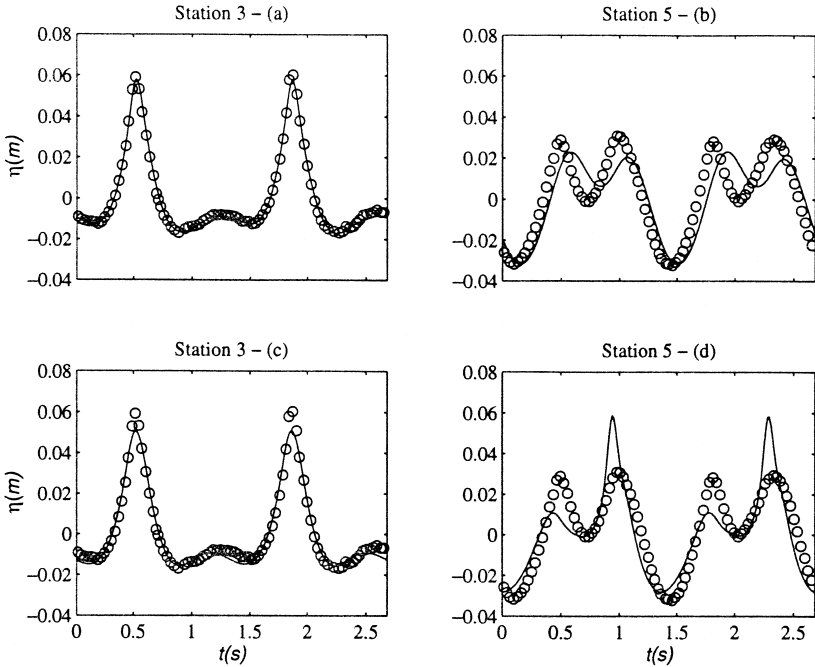


Fig. 12. Comparisons of free surface displacement with case (2) of the Ohyama experimental data at stations 3 and 5. FN4 (upper panels—a,b), WKGS (lower panels—c,d), data (circles).

experimental setup. The wave flume is 65 m long and 1.0 m wide. The total depth of the flume is 1.6 m. The location of the center of the bar was 28.3 m from the piston-type wavemaker. All other relevant dimensions can be seen in Fig. 11. The measurements were performed before the point when waves reflected from the bar reached the wavemaker.

At the right end of the flume, waves were absorbed by the presence of coarse materials to dissipate the energy. A total of six tests were performed with three different incident wave periods (1.34 s, 2.01 s, 2.68 s) each for two different wave amplitudes (0.0125 m, 0.025 m). No wave breaking occurred in any of the tests. The data was obtained by digitization of the plots from the original article. The only time series available for comparisons were the ones at stations 3 and 5, for all three wave periods, and the highest of the two amplitudes (0.025 m). Fourier amplitudes were available for the same wave conditions but at all measurement stations. Time series were synchronized at station 3.

It is not clear from Ohyama et al., 1994 that the measurements shown in the paper were performed after the waves had reached a permanent form, but we are assuming this is the case. The models' results were taken after a steady wave was reached at station 5.

We refer to the three tests as cases (2), (4), and (6), as in Ohyama et al. (1994). The incident wave conditions are summarized in Table 3. The incident wave conditions are similar in the Ohyama and Delft experiments. The major difference between the two

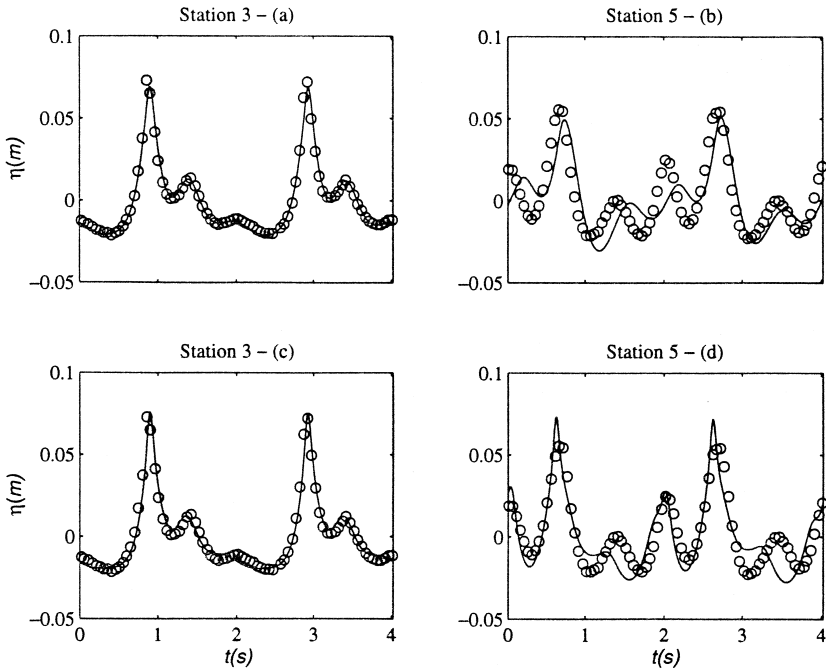


Fig. 13. Comparisons of free surface displacement with case (4) of the Ohyama experimental data at stations 3 and 5. FN4 (upper panels—a,b), WKGS (lower panels—c,d), data (circles).

experiments is that the bar in the Ohyama experiment is much shorter and with much steeper slopes than the one in the Delft experiments, more reminiscent of a submerged rubble mound structure. The steep slopes add extra difficulty for the models' performance, since: (i) the models' dispersion properties are optimized assuming constant depth; (ii) the assumption that the vertical velocity is $O(\mu^2)$ times the horizontal velocity is violated at steep slopes. Smoothing of the corners of the bar, besides filtering every 100 time steps was necessary to prevent spurious high frequency noise to contaminate the solutions. To smooth the corners of the bar we applied a 3-point average by Shapiro (1970) five times. Since the waves are progressively longer from cases (2) through (6), we expect that the Boussinesq models will perform best in case (6), and worst in case (2). We also expect higher mismatches between models and data at station 5 than at station 3, due to increasing errors in the phase of the decomposed higher frequency bound waves as they reach the deeper water behind the bar.

Figs. 12–14 show comparisons of the FN4 and WKGS models with data for cases (2), (4), and (6), respectively. Notice that for cases (2) and (4) the FN4 model shows a mismatch in the phase speed at station 5, and an underprediction of the wave crests and troughs, an indication that even the fully nonlinear, $O(\mu^4)$ model has limited ability to predict waves past a submerged bar with very steep slopes, if the waves are short enough. For case (6) the FN4 model agrees very well with the data. For all three cases,

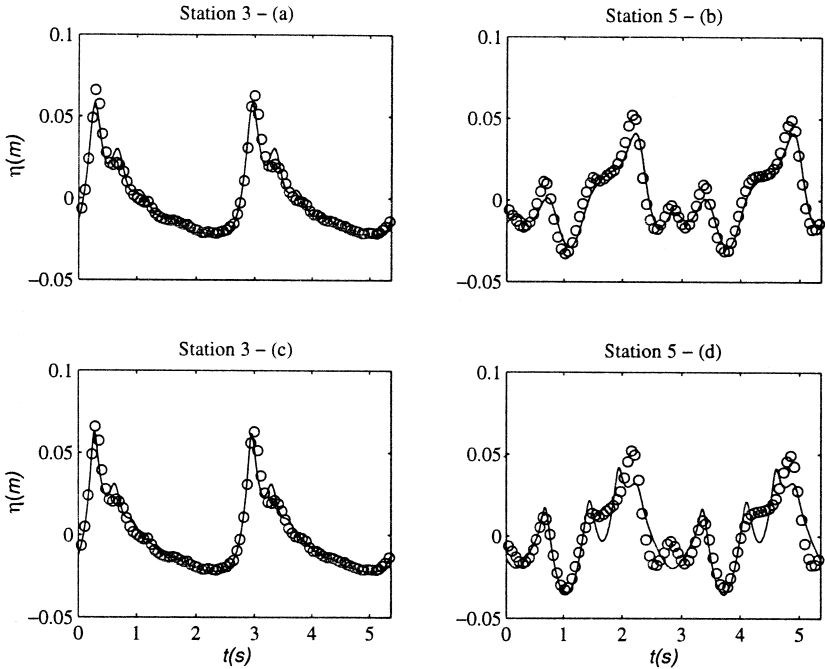


Fig. 14. Comparisons of free surface displacement with case (6) of the Ohyama experimental data at stations 3 and 5. FN4 (upper panels—*a,b*), WKGS (lower panels—*c,d*), data (circles).

the WKGS model has poor qualitative agreement with the data at station 5, mostly due to phase errors and overprediction of higher harmonics behind the bar.

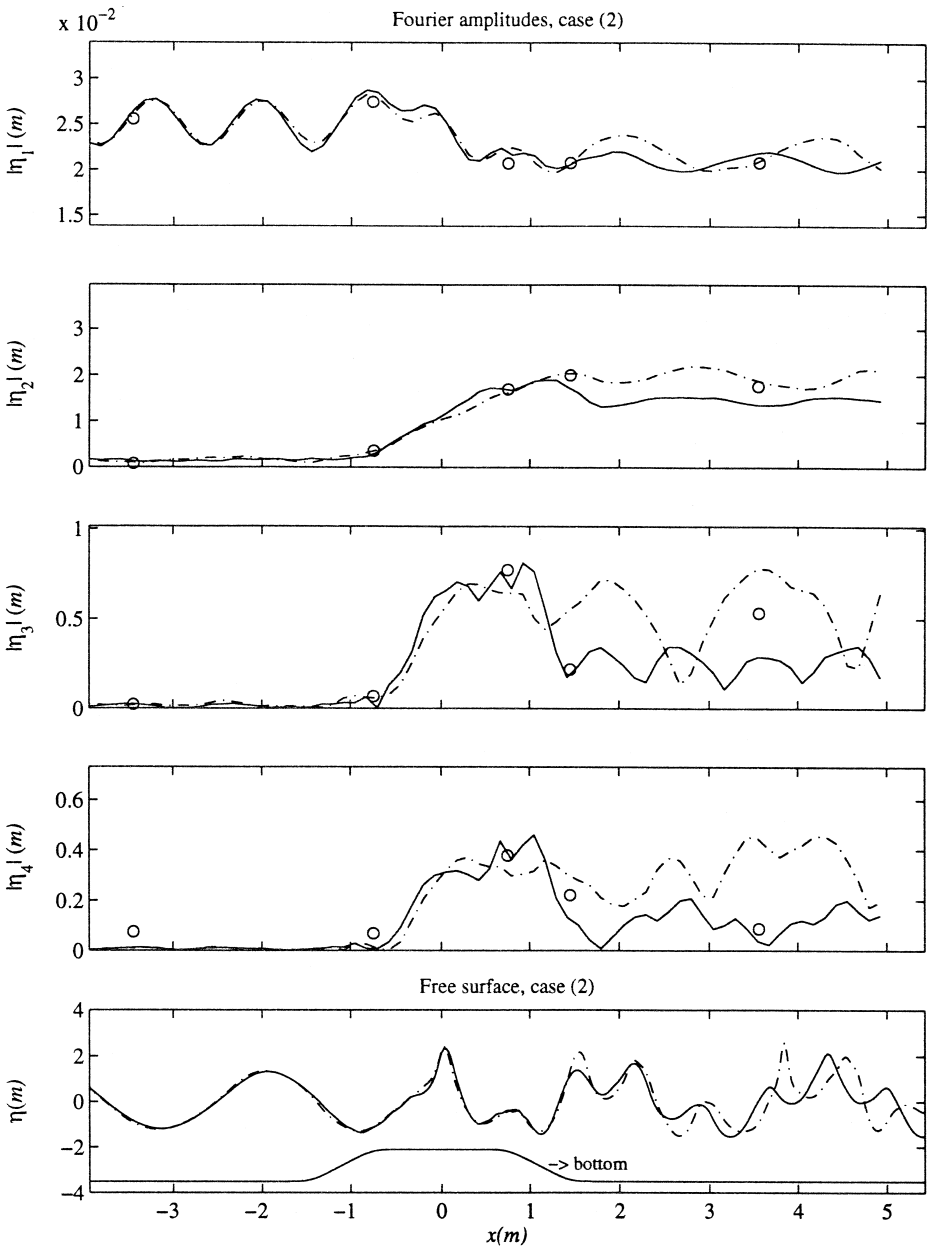


Fig. 15. Comparisons of the spatial variation of the Fourier components of the free surface displacement with case (2) of the Ohyama experimental data. Bottom panel shows the free surface elevation. FN4 (solid), WKGS (dash-dot), data (circles).

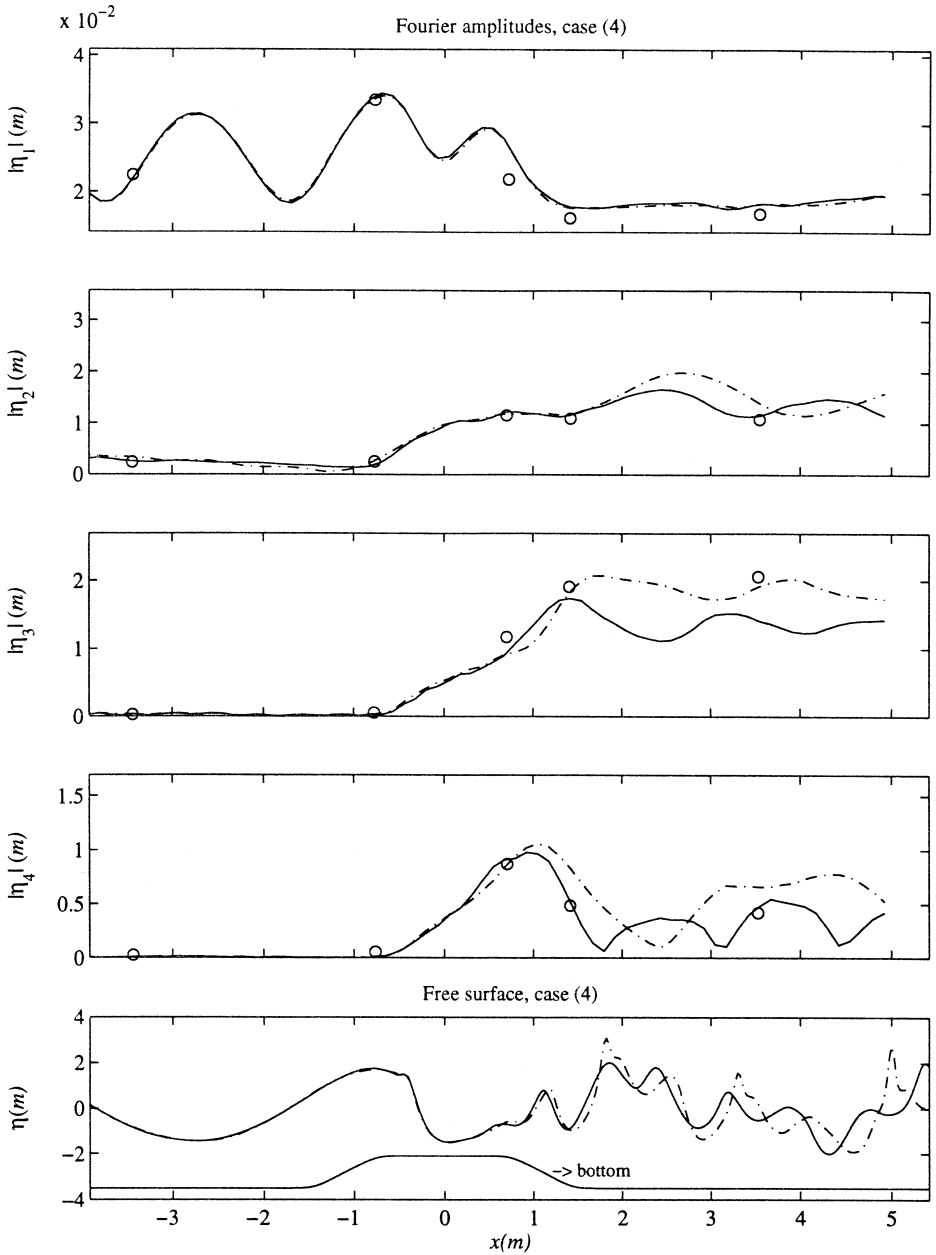


Fig. 16. Comparisons of the spatial variation of the Fourier components of the free surface displacement with case (4) of the Ohyama experimental data. Bottom panel shows the free surface elevation. FN4 (solid), WKGS (dash-dot), data (circles).

Figs. 15–17 show comparisons of the Fourier amplitudes along the flume between both FN4 and WKGS, and the data points at each station for cases (2), (4), and (6),

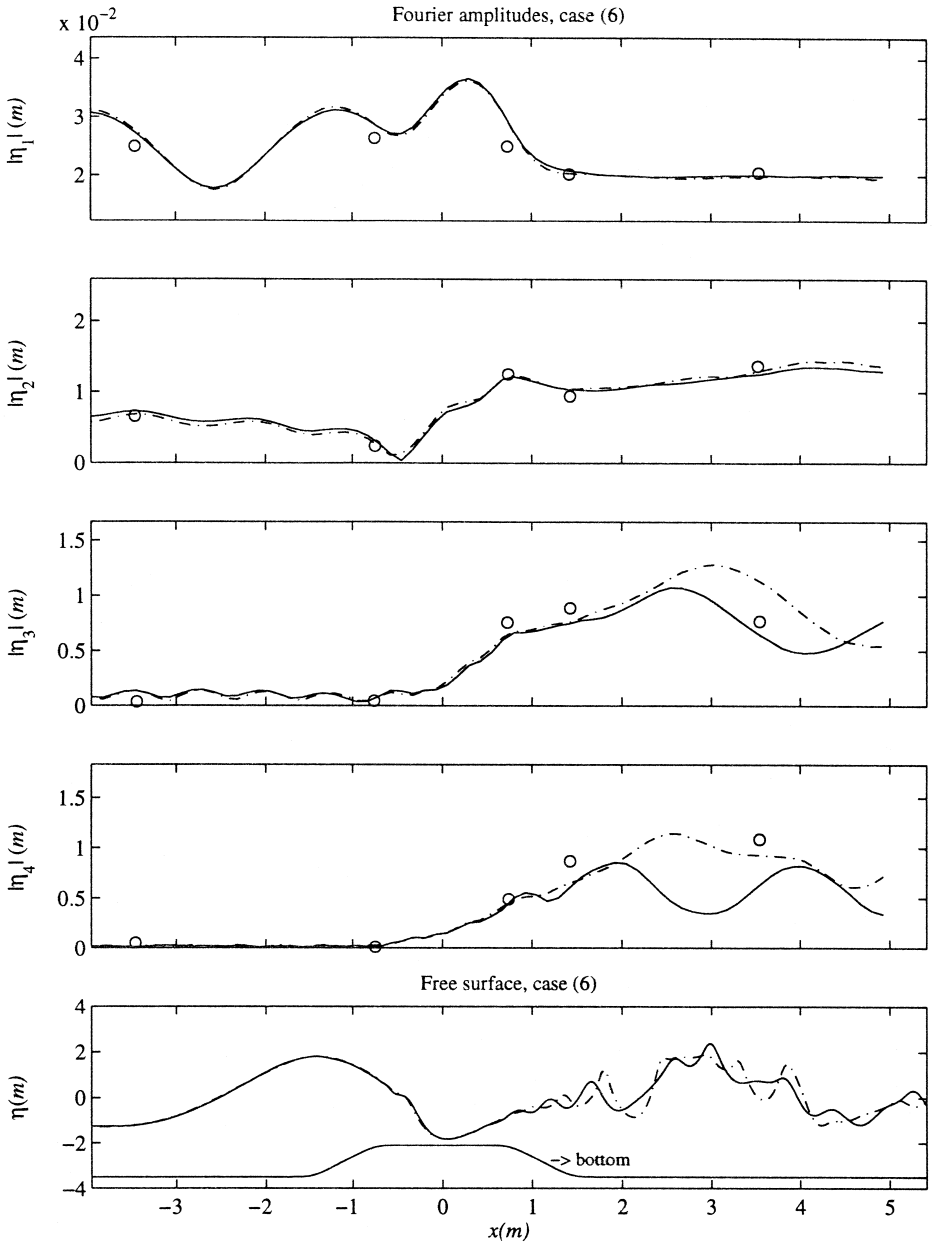


Fig. 17. Comparisons of the spatial variation of the Fourier components of the free surface displacement with case (6) of the Ohyama experimental data. Bottom panel shows the free surface elevation. FN4 (solid), WKGS (dash-dot), data (circles).

Table 4
Index of agreement d_i

Station	Case (2)		Case (4)		Case (6)	
	WKGS	FN4	WKGS	FN4	WKGS	FN4
3	0.994	0.998	0.991	0.994	0.991	0.991
5	0.921	0.914	0.927	0.880	0.945	0.976

respectively. In all cases, the models predict well the Fourier amplitudes before the back face of the bar. For case (2), WKGS gives slightly better prediction of the second harmonic at stations 4 and 5 than FN4, but once again strongly overpredicts the third and fourth harmonics at those stations. For case (4), the FN4 model gives better prediction than WKGS for all but the third harmonic, which WKGS agrees slightly better with the data. For case (6), both models agree reasonably well with the data, with FN4 having a better prediction of the third harmonic at station 5 and the WKGS model matching the fourth harmonic slightly better at that same station. For this case, the deviations from the data in the time series computed by WKGS at station 5 are probably due to phase errors, which is not detected by the Fourier amplitudes comparisons.

Table 4 shows the index of agreement between WKGS and FN4, and the data from the Ohyama experiment for cases (2), (4), and (6), stations 3 and 5. Notice that for cases (2) and (4), the results indicate a better agreement with the data by WKGS than by FN4. By inspecting time series in Figs. 12 and 13, it is clear that the better agreement index for WKGS is only due to a systematic phase error by FN4, which, overall has a better qualitative agreement.

5. Conclusions

A Boussinesq-type model (FN4) with $O(1)$ nonlinearity and $O(\mu^4)$ dispersion and vertical dependence was developed for surface water wave propagation over uneven beds in two horizontal dimensions. The model is the extension of Gobbi et al. (1998b) to include variable bottom topography.

A numerical implementation of the 1-D version of the model was used to simulate wave evolution over arbitrary bottom topography. The numerical model included absorbing sponge layers to simulate radiation boundary conditions, and generation of waves inside the domain by the inclusion of a source function in the system of equations. In comparison with $O(\mu^2)$ models, the extra computational cost of the FN4 model is mostly due to the much greater number of terms. We believe that an optimization of the code for parallel processing machines would make it only marginally less efficient than $O(\mu^2)$ models. This and a 2-D numerical implementation of the model are the author's goals for future work.

Computations with FN4 and WKGS were compared to several laboratory measurements of waves propagating over submerged sills, and FN4 generally gave better agreement with the data. The weakly nonlinear version of the model, WN4, was also

compared to some of the data. The results showed that the nonlinear terms neglected in WN4 are essential for accurate prediction of the generation of higher harmonics of shoaling waves.

Results from the present study are compared to results from several levels of the local polynomial approximation (LPA) method of Kennedy and Fenton (1997) in Gobbi et al. (1998a). FN4 is found to perform as well or better than LPA models with a similar degree of polynomial approximation over the water column, and compares favorably with LPA with $n = 7$ (corresponding to a sixth degree polynomial in the vertical direction) in many cases.

Acknowledgements

This work has been supported by the brazilian agency Fundação CAPES, and by the US Army Research Office through University Research Initiative grant DAAL 03-92-G-0116. A table of data digitized from Ohyama et al.’s original figures was provided by Dr. Andrew Kennedy. Dr. Maarten Dingsmans provided the results of Delft Hydraulics tests.

Table 5
Coefficients in the finite difference formulas for the spatial derivatives

γ	$K_{i \mp 3}$	$K_{i \mp 2}$	$K_{i \mp 1}$	K_i	$K_{i \pm 1}$	$K_{i \pm 2}$	$K_{i \pm 3}$	Error	
<i>O(1)</i>									
\tilde{u}_{xi}	$\pm(60\Delta x)^{-1}$	-1	9	-45	0	45	-9	1	$O(\Delta x^6)$
$\tilde{u}_{xi \mp 1}$	$\pm(60\Delta x)^{-1}$	2	-24	- 35	80	-30	8	-1	$O(\Delta x^6)$
$\tilde{u}_{xi \mp 2}$	$\pm(60\Delta x)^{-1}$	-10	- 77	150	-100	50	-15	2	$O(\Delta x^6)$
\tilde{u}_{xxi}	$(180\Delta x^2)^{-1}$	2	-27	270	- 490	270	-27	2	$O(\Delta x^6)$
$\tilde{u}_{xxi \mp 1}$	$(180\Delta x^2)^{-1}$	-13	288	- 420	200	15	-12	2	$O(\Delta x^5)$
$\tilde{u}_{xxi \mp 2}$	$(180\Delta x^2)^{-1}$	137	- 147	-255	470	-285	93	-13	$O(\Delta x^5)$
<i>O(μ^2)</i>									
\tilde{u}_{xi}	$\pm(12\Delta x)^{-1}$	-	1	-8	0	8	-1	-	$O(\Delta x^4)$
$\tilde{u}_{xi \pm 1}$	$\pm(12\Delta x)^{-1}$	-	-3	- 10	18	-6	1	-	$O(\Delta x^4)$
\tilde{u}_{xxi}	$(12\Delta x^2)^{-1}$	-	-1	16	- 30	16	-1	-	$O(\Delta x^4)$
$\tilde{u}_{xxi \mp 1}$	$(12\Delta x^2)^{-1}$	-	11	- 20	6	4	-1	-	$O(\Delta x^3)$
$\tilde{u}_{xxx i}$	$\pm(8\Delta x^3)^{-1}$	1	-8	13	0	-13	8	-1	$O(\Delta x^4)$
$\tilde{u}_{xxx i \mp 1}$	$\pm(8\Delta x^3)^{-1}$	-1	-8	35	-48	29	-8	1	$O(\Delta x^4)$
$\tilde{u}_{xxx i \mp 2}$	$\pm(8\Delta x^3)^{-1}$	-15	56	-83	64	-29	8	-1	$O(\Delta x^4)$
<i>O(μ^4)</i>									
\tilde{u}_{xi}	$\pm(2\Delta x)^{-1}$	-	-	-1	0	1	-	-	$O(\Delta x^2)$
\tilde{u}_{xxi}	$(\Delta x^2)^{-1}$	-	-	1	2	1	-	-	$O(\Delta x^2)$
$\tilde{u}_{xxx i}$	$\pm(2\Delta x^2)^{-1}$	-	-1	2	0	-2	1	-	$O(\Delta x^2)$
$\tilde{u}_{xxx i \mp 1}$	$\pm(2\Delta x^2)^{-1}$	-	-3	10	-12	6	-1	-	$O(\Delta x^2)$
$\tilde{u}_{xxxx i}$	$(\Delta x^4)^{-1}$	-	1	-4	6	-4	1	-	$O(\Delta x^2)$
$\tilde{u}_{xxxx i \mp 1}$	$(\Delta x^4)^{-1}$	-	1	-4	6	-4	1	-	$O(\Delta x)$

Appendix A. Numerical spatial derivatives

The spatial derivatives appearing in Eqs. (47) and (48) are evaluated according to the condition that the errors be smaller than $O(\mu^4)$ when we assume $k\Delta x = O(\mu)$, which amounts to the use of schemes such that the $O(\mu^p)$ terms contain truncation errors of $O(\Delta x^{(5-p)})$ or higher. The finite difference formulas for the spatial derivatives of say \tilde{u} can be written as:

$$\mathcal{D}\tilde{u}_l = \gamma \sum_{n=i-m}^{i+m} K_n \tilde{u}_n, \tag{75}$$

where $\mathcal{D}\tilde{u}_l$ are derivatives of \tilde{u} with respect to x at location l ($i - m + 1 \leq l \leq i + m - 1$), $l = i$ are centered derivatives, and $l \neq i$ are off-centered derivatives (near the boundaries). m can be either 1, 2, or 3, depending on the truncation error, and γK_n are the coefficients of \tilde{u}_n . Table 5 shows the values of γ and K_n for the \mathcal{D}_l derivatives appearing in the $O(1)$, $O(\mu^2)$, and $O(\mu^4)$ terms (first column). The \pm and \mp signs are used so that the formulas for the off-centered derivatives can be applied to both near-the-left and near-the-right boundaries. The coefficients in boldface indicate the point where the derivatives are computed. The numerical truncation errors are shown in the last column.

Appendix B. Derivation of source function

Here we derive the x -direction source function for regular waves. The linearized versions of the mass and momentum equations for $\tilde{\phi}$ over a flat bottom, including the source function is given, in dimensional form, as:

$$\eta_t + h\nabla^2 \tilde{\phi} - C_1 h^3 \nabla^2 \nabla^2 \tilde{\phi} + C_2 h^5 \nabla^2 \nabla^2 \nabla^2 \tilde{\phi} = f_s(x, y, t), \tag{76}$$

$$\tilde{\phi}_t + g\eta - C_3 h^2 \nabla^2 \tilde{\phi}_t + C_4 h^4 \nabla^2 \nabla^2 \tilde{\phi}_t = 0, \tag{77}$$

where coefficients C_1, C_2, C_3, C_4 are given by

$$C_1 = -\frac{1}{2}(B - 1/3), \tag{78}$$

$$C_2 = \frac{1}{4}(B^2 - B/3 - D/6 + 1/30), \tag{79}$$

$$C_3 = -\frac{1}{2}(B - 1), \tag{80}$$

$$C_4 = \frac{1}{4}(B^2 - B - D/6 + 1/6). \tag{81}$$

Taking the t derivative of the momentum equation and eliminating η from Eqs. (76) and (77), gives:

$$\begin{aligned} \tilde{\phi}_{tt} - gh\nabla^2 \tilde{\phi} + C_1 gh^3 \nabla^2 \nabla^2 \tilde{\phi} - C_2 gh^5 \nabla^2 \nabla^2 \nabla^2 \tilde{\phi} - C_3 h^2 \nabla^2 \tilde{\phi}_{tt} \\ + C_4 h^4 \nabla^2 \nabla^2 \tilde{\phi}_{tt} = -gf_s(x, y, t). \end{aligned} \tag{82}$$

We introduce the following transformations:

$$\tilde{\phi}(x, y, t) = \left(\frac{1}{2\pi}\right)^2 \int_{-\infty}^{+\infty} \int_{-\infty}^{+\infty} \hat{\phi}(x) e^{i\lambda y} e^{-i\omega t} d\lambda d\omega \quad (83)$$

$$f(x, y, t) = \left(\frac{1}{2\pi}\right)^2 \int_{-\infty}^{+\infty} \int_{-\infty}^{+\infty} \hat{f}(x) e^{i\lambda y} e^{-i\omega t} d\lambda d\omega. \quad (84)$$

Substituting Eqs. (83) and (84) into Eq. (82), we have:

$$a\hat{\phi}^{[6]} + b\hat{\phi}^{[4]} + c\hat{\phi}^{[2]} + d\hat{\phi} = g\hat{f}, \quad (85)$$

where the numbers in brackets denote order of x derivatives, and

$$a \equiv C_2 gh^5, \quad (86)$$

$$b \equiv -C_1 gh^3 + C_4 h^4 \omega^2 - 3C_2 gh^5 \lambda^2, \quad (87)$$

$$c \equiv gh - C_3 h^2 \omega^2 + 2C_1 gh^3 \lambda^2 - 2C_4 h^4 \lambda^2 \omega^2 + 3C_2 gh^5 \lambda^4, \quad (88)$$

$$d \equiv \omega^2 - gh\lambda^2 + C_3 h^2 \lambda^2 \omega^2 - C_1 gh^3 \lambda^4 + C_4 h^4 \lambda^4 \omega^2 - C_2 gh^5 \lambda^6. \quad (89)$$

Now we multiply Eq. (85) by a Green's function $G(\xi, x)$, and integrate the product with respect to ξ , from $-\infty$ to $+\infty$, which gives:

$$\begin{aligned} & \int_{-\infty}^{+\infty} (aG^{[6]} + bG^{[4]} + cG^{[2]} + dG) \hat{\phi} d\xi + a[G\hat{\phi}^{[5]} - G^{[1]}\hat{\phi}^{[4]} + G^{[2]}\hat{\phi}^{[3]} \\ & - G^{[3]}\hat{\phi}^{[2]} + G^{[4]}\hat{\phi}^{[1]} + G^{[5]}\hat{\phi}]_{-\infty}^{+\infty} + b[G\hat{\phi}^{[3]} - G^{[1]}\hat{\phi}^{[2]} + G^{[2]}\hat{\phi}^{[1]} \\ & - G^{[3]}\hat{\phi}]_{-\infty}^{+\infty} + c[G\hat{\phi}^{[1]} - G^{[1]}\hat{\phi}]_{-\infty}^{+\infty} = g \int_{-\infty}^{+\infty} G\hat{f} d\xi, \end{aligned} \quad (90)$$

where the numbers in brackets denote order of ξ derivatives. Notice that ξ is a dummy variable and x is now an arbitrary fixed point in the ξ coordinate. Following the traditional Green's function theory, we seek a solution such that:

$$aG^{[6]} + bG^{[4]} + cG^{[2]} + dG = \delta(\xi - x), \quad (91)$$

with boundary conditions such that all boundary terms in Eq. (90) are eliminated:

$$G^{[n]} \rightarrow (\pm il)^n G, \quad \hat{\phi}^{[n]} \rightarrow (\pm il)^n \hat{\phi}; \quad n = 1, \dots, 5, \quad x \rightarrow \pm\infty, \quad (92)$$

where $\delta(\xi - x)$ is the Dirac delta function at $\xi = x$. We are interested in solutions where $a \neq 0$. By integrating Eq. (91) just across $\xi = x$, from $x - \epsilon$ to $x + \epsilon$ ($\epsilon \rightarrow 0$), and requiring continuity of $G, G^{[1]}, G^{[2]}, G^{[3]}, G^{[4]}$, we are left with:

$$aG^{[5]} \Big|_{x-\epsilon}^{x+\epsilon} = 1. \quad (93)$$

Away from $\xi = x$ we, can write:

$$G^{[6]} + a_1 G^{[4]} + a_2 G^{[2]} + a_3 G = 0, \quad (94)$$

where $a_1 = b/a, a_2 = c/a, a_3 = d/a$. Seeking a solution of the form:

$$G \sim e^{i\sigma\xi}, \quad (95)$$

we obtain the characteristic polynomial:

$$\sigma^6 - a_1\sigma^4 - a_2\sigma^2 - a_3 = 0. \tag{96}$$

For the case in which we are interested, the roots of Eq. (96) can be written as:

$$\sigma_1 = -\sigma_4 = l, \tag{97}$$

$$\sigma_2 = -\sigma_5 = iL_1, \tag{98}$$

$$\sigma_3 = -\sigma_6 = iL_2, \tag{99}$$

where l, L_1, L_2 are positive real numbers, and can be obtained from the roots of the bi-cubic polynomial Eq. (96). We now write the solution for the source function:

$$G(\xi, x) = \begin{cases} G_+ = A_G e^{i l(\xi-x)} + B_G e^{L_1(\xi-x)} + C_G e^{L_2(\xi-x)} & \text{if } \xi < x, \\ G_- = A_G e^{i l(x-\xi)} + B_G e^{L_1(x-\xi)} + C_G e^{L_2(x-\xi)} & \text{if } \xi > x. \end{cases} \tag{100}$$

Continuity of $G, G^{[2]}, G^{[4]}$ are satisfied automatically, as are the boundary conditions at $\pm\infty$. Continuity of $G^{[1]}, G^{[3]}$, and substitution of Eq. (100) into Eq. (93) gives three equations for the three unknowns $A_G, B_G,$ and $C_G,$ the solution being:

$$A_G = \frac{-i}{2al(l^2 + L_1^2)(l^2 + L_2^2)}, \tag{101}$$

$$B_G = \frac{1}{2al(l^2 + L_1^2)(L_1^2 - L_2^2)}, \tag{102}$$

$$C_G = \frac{1}{2al(l^2 + L_2^2)(L_2^2 - L_1^2)}. \tag{103}$$

Eq. (101) can be rearranged to give:

$$A_G = \frac{-il}{2(2l^6 - a_1l^4 + a_3)}. \tag{104}$$

From Eq. (90), we can write:

$$\begin{aligned} \hat{\phi}(x) &= \int_{-\infty}^{+\infty} G(\xi, x) g\hat{f}(\xi) d\xi = \int_{-\infty}^x G_-(\xi, x) g\hat{f}(\xi) d\xi \\ &+ \int_x^{+\infty} G_+(\xi, x) g\hat{f}(\xi) d\xi. \end{aligned} \tag{105}$$

We arbitrarily choose:

$$\hat{f}(x) = D_s \exp(-\beta_s x^2). \tag{106}$$

For sufficiently large values of x (progressive wave traveling to greater values of x), and using Eq. (104):

$$\hat{\phi}(x) = \int_{-\infty}^x G_-(\xi, x) g\hat{f}(\xi) d\xi = gD_s [A_G I_1 e^{ilx} + B_G I_2 e^{-L_1 x} + C_G I_3 e^{-L_2 x}], \tag{107}$$

where

$$I_1 = \int_{-\infty}^{+\infty} \exp(-\beta_s x^2 - ilx) dx = \sqrt{\frac{\pi}{\beta_s}} \exp\left(-\frac{l^2}{4\beta_s}\right), \quad (108)$$

$$I_2 = \int_{-\infty}^{+\infty} \exp(-\beta_s x^2 + L_1 x) dx = \sqrt{\frac{\pi}{\beta_s}} \exp\left(\frac{L_1^2}{4\beta_s}\right), \quad (109)$$

$$I_3 = \int_{-\infty}^{+\infty} \exp(-\beta_s x^2 + L_2 x) dx = \sqrt{\frac{\pi}{\beta_s}} \exp\left(\frac{L_2^2}{4\beta_s}\right). \quad (110)$$

Terms involving I_2 and I_3 become negligibly small as $x \rightarrow \infty$, so:

$$\hat{\phi}(x) \approx gD_s A_G I_1 e^{ilx}. \quad (111)$$

We here are interested in waves propagating in the x direction. The desired progressive wave solution (waves propagating in x) of Eqs. (76) and (77) away from the source region ($x \rightarrow \infty$) is:

$$\eta = \eta_0 e^{i(kx - \omega t)}, \quad (112)$$

$$\tilde{\phi} = \tilde{\phi}_0 e^{i(kx - \omega t)}, \quad (113)$$

$$\tilde{\phi}_0 = \frac{ig\eta_0}{\omega \left[1 + C_3(kh)^2 + C_4(kh)^4 \right]}, \quad (114)$$

$$\omega^2 = gk^2 h \frac{1 + C_1(kh)^2 + C_2(kh)^4}{1 + C_3(kh)^2 + C_4(kh)^4}. \quad (115)$$

Setting $\lambda = 0$ (no y dependence) and $l = k$ we can write:

$$\tilde{\phi}(x, y, t) = gD_s A_G I_1 e^{i(kx - \omega t)}. \quad (116)$$

Substitution of Eqs. (113) and (114) into Eq. (116), gives the relationship between the source function amplitude D_s and the desired wave amplitude η_0 :

$$D_s = \frac{i\eta_0}{\omega A_G I_1 \left[1 + C_3(kh)^2 + C_4(kh)^4 \right]}. \quad (117)$$

References

- Beji, S., Battjes, J.A., 1993. Experimental investigations of wave propagation over a bar. *Coastal Engineering* 19 (1–2), 151–162.
- Chen, Q., Dalrymple, R.A., Kirby, J.T., Kennedy, A., Haller, M.C., 1999. Boussinesq modelling of a rip current system. *J. Geophys. Res.*, submitted.
- Dingemans, M.W., 1994. Comparison of computations with Boussinesq-like models and laboratory measurements. Report H-1684.12, Delft Hydraulics, 32 pp.
- Gobbi, M.F., 1998. A new Boussinesq-type model for surface water wave propagation. Dissertation, University of Delaware.

- Gobbi, M.F., Kennedy, A.B., Kirby, J.T., 1998a. A comparison of higher-order Boussinesq and local polynomial approximation models. In Proc. 26th Intl. Conf. Coastal Eng., Copenhagen, presented.
- Gobbi, M.F., Kirby, J.T., Wei, G., 1998b. A fully nonlinear Boussinesq model for surface waves: Part II. Extension to $O(kh)^4$. J. Fluid Mech., submitted.
- Kennedy, A.B., Fenton, J.D., 1997. A fully-nonlinear computational method for wave propagation over topography. Coastal Engineering 32, 137–161.
- Kirby, J.T., Wei, G., 1994. Derivation and properties of a fully nonlinear, extended Boussinesq model. In Proc. IAHR Symposium: Waves—Phys. and Num. Model., Vancouver, pp. 386–395.
- Larsen, J., Dancy, H., 1983. Open boundaries in short-wave simulations—a new approach. Coastal Engineering 7, 285–297.
- Luth, H.R., Klopman, G., Kitou, N., 1994. Kinematics of waves breaking partially on an offshore bar; LDV measurements of waves with and without a net onshore current. Report H-1573, Delft Hydraulics, 40 pp.
- Madsen, P.A., Sørensen, O.R., 1992. A new form of Boussinesq equations with improved linear dispersion characteristics: Part 2. A slowly-varying bathymetry. Coastal Engineering 18, 183–204.
- Madsen, P.A., Murray, R., Sørensen, O.R., 1991. A new form of Boussinesq equations with improved linear dispersion characteristics. Coastal Engineering 15, 371–388.
- Madsen, P.A., Sørensen, O.R., Schäffer, H.A., 1997a. Surf zone dynamics simulated by a Boussinesq type model: Part 1. Model description and cross-shore motion of regular waves. Coastal Engineering 32, 255–287.
- Madsen, P.A., Sørensen, O.R., Schäffer, H.A., 1997b. Surf zone dynamics simulated by a Boussinesq type model: Part 2. Surf beat and swash oscillations for wave groups and irregular waves. Coastal Engineering 32, 289–319.
- Nwogu, O., 1993. An alternative form of the Boussinesq equations for nearshore wave propagation. J. Waterway, Port, Coast., Ocean Eng. 119, 618–638.
- Ohyama, T., Kiota, W., Tada, A., 1994. Applicability of numerical models to nonlinear dispersive waves. Coastal Engineering 24, 213–297.
- Shapiro, R., 1970. Smoothing, filtering and boundary effects. Geophys. Space Phys. 8 (2), 359–387.
- Sørensen, O.R., Schäffer, H.A., Madsen, P.A., 1998. Surf zone dynamics simulated by a Boussinesq type model: III. Wave-induced horizontal nearshore circulations. Coastal Engineering 33, 155–176.
- Tanaka, M., 1986. The stability of solitary waves. Phys. Fluids 29, 650–655.
- Wei, G., 1997. Simulation of water waves by Boussinesq models. Dissertation, University of Delaware, 202 pp.
- Wei, G., Kirby, J.T., 1995. Time-dependent numerical code for extended Boussinesq equations. J. Waterway, Port, Coast., Ocean Eng. 121, 251–261.
- Wei, G., Kirby, J.T., Grilli, S.T., Subramanya, R., 1995. A fully nonlinear Boussinesq model for surface waves: Part 1. Highly nonlinear unsteady waves. J. Fluid Mech. 294, 71–92.
- Wei, G., Kirby, J.T., Sinha, A., 1999. Generation of waves in Boussinesq models using a source function method. Coastal Engineering 36, 271–299.
- Wilmott, C.J., 1981. On the validation of models. Physical Geography 2 (2), 219–232.